MPPT Design and Implementation based on c-RIME Optimizer for Hybrid PV-TEG System

Jingbo Wang[a], Shaocong Wu[b], Bo Yang [b], Lin Jiang[a,*]

[a] Department of Electrical Engineering and Electronics, University of Liverpool, L69 3GJ Liverpool, United Kingdom;

[b] Faculty of Electric Power Engineering, Kunming University of Science and Technology, 650500 Kunming, China.

* Corresponding author: Lin Jiang, E-mail: ljiang@liverpool.ac.uk

Abstract: To reduce reliance on fossil fuels and promote sustainable energy production, a hybrid photovoltaic-thermoelectric generator (PV-TEG) system is devised in this study to realize efficient and cyclic utilization of green energy. Nevertheless, the real-world operational environment inevitably results in partial shading condition (PSC) and non-uniform temperature distribution (NTD) across PV and TEG modules, which adversely distorts their operational characteristics and then compromises efficiency for available captured power. To address this, a highly efficient maximum power extraction strategy based on a chaotic rime optimization algorithm (c-RIME) is developed to dynamically realize maximum power point tracking (MPPT) under diverse operation scenarios. Despite several studies on MPPT for hybrid PV-TEG systems, all have only focused on technical performance such as power enhancement, while neglecting critical environmental analysis which is actually the motivation for developing these renewable technologies. Therefore, to address this gap, this work aims to undertake a systematic analysis covering both technical and sustainability assessment. Meanwhile, compared with existing research, more complex and realistic operational scenarios are considered in case studies, especially utilizing the real-world field-measured datasets from Hong Kong and Ningxia for technical and environmental evaluation, respectively. Simulation results demonstrate that c-RIME based MPPT technique can achieve the highest output energy (up to 126.67%) compared with prior studies under all testing scenarios while contributing to considerable carbon emissions reduction.

Keywords: Hybrid PV-TEG system, Techno-environmental assessment, Maximum power point tracking, Partial shading conditions, Non-uniform temperature distribution, Rime optimization algorithm

Nomenclature

Variables		T_{op}	Operating temperature of TEG, °C
V_{PV}	PV output voltage, V	G_T	Solar irradiance intensity, W/m^2
I_{PV}	PV output current, A	T_{am}	Ambient temperature, °C
I_b	PV cell's photocurrent, A	W_s	Wind speed, m/s
I_s	PV cell's reverse saturation current, A	S_{PV}	PV board area, m^2
T_{ca}	PV cell's absolute working temperature, °C	***Abbreviations***	
N_p	Quantity of PV modules arranged in parallel	**AOA**	Arithmetic optimization algorithm
N_s	Quantity of PV modules arranged in series	**AOS**	Atomic orbital search optimization
$V_{reverse}$	Shaded cell's reverse voltage, V	**CCUS**	Carbon capture, utilization, and storage
V_{Bdiode}	Bypass diode's voltage drop, V	**c-RIME**	Chaotic rime optimization algorithm
P_{TEG}	TEG system output power, W	**CS**	Cuckoo search
P_{PV}	PV system output power, W	**GMPP**	Global maximum power points
V_{oc}	Open-circuit voltage, V	**GWO**	Grey wolf optimizer

R_{TEG}	Internal resistance of TEG, Ω	**IGBT**	Insulated gate bipolar transistor
R_L	Resistance of load of TEG, Ω	**INC**	Incremental conductance method
V_{oci}	Open-circuit voltage of the *i*th TEG module, V	**LCA**	Life cycle assessment
I_{sci}	Short-circuit current of the *i*th TEG module, A	**LMPP**	Local maximum power point
V_{Li}	Terminal voltage of the *i*th TEG module, V	**MFO**	Moth-flame optimization
R_{TEGi}	Internal resistance of the *i*th TEG module, Ω	**MPPT**	Maximum power point tracking
P_{TEGi}	Output power of the *i*th TEG, W	**MVO**	Multi-verse optimization
$P_{TEG\Sigma}$	Overall power output produced by the TEG system, W	**NTD**	Non-uniform temperature distribution
$P_{PV\text{-}TEG}$	Output power of the PV-TEG hybrid system, W	**P&O**	Perturb and observe
η_{pv-teg}	Energy generation efficiency of hybrid PV-TEG systems	**PSC**	Partial shading condition
PV-TEG hybrid system parameters		***P-T***	Power-temperature
q	Electron charge, $1.60217733 \times 10^{-19}$ Cb	**PV**	Photovoltaic
A	Ideality factor of p-n junction	**PV-TEG**	Photovoltaic-thermoelectric generator
K	Boltzman's constant, 1.380658×10^{-23} J/K	***P-V***	Power-voltage
α	Seebeck coefficient, μV/K	**RIME**	Rime optimization algorithm
T_h	Hot side temperature, °C	**RSA**	Reptile search algorithm
T_c	Cold side temperature, °C	**SCA**	Sine cosine algorithm
ΔT	Temperature difference between hot and cold sides, °C	**SP**	Series-parallel
T_{av}	Average temperature of hot and cold sides, °C	**SSA**	Salp swarm algorithm
α_0	Essential element of Seebeck coefficient, μV/K	**TCT**	Total-cross-tied
α_1	Seebeck coefficient variation rate, μV/K	**TEG**	Thermoelectric generator

1. Introduction

A broad consensus has been reached on global action to address climate change, and most countries around the world have set clear targets for carbon neutrality [1]. The target of the Net Zero emissions by 2050 scenario contributes to promoting the optimization and upgrading of the economic, energy, and industrial structures, and accelerating the promotion of energy transformation [2]. In this context, the renewable energy industry, as a major measure to optimize the industrial structure, needs to promote its innovative development and establish the efficient utilization of resources as well as the green low-carbon development path [3]. A variety of renewable resources such as solar, wind, ocean, and thermal energy have achieved breakthrough development in recent years [4], entering a new stage of high-quality development. In particular, the photovoltaic (PV) system witnesses a large variety of applications thanks to its prominent advantages of abundant resources, pollution-free, and low cost [5]. However, there are also two distinctive shortcomings regarding its power generation, (a) relatively low solar energy density and (b) vulnerability to varying meteorological factors (e.g., season, location, climate).

During the photo-electric conversion, a large proportion of absorbed solar energy is dissipated as thermal waste [6]. According to the investigation in literature [7], roughly 83% of the incident solar irradiance is transformed into heat within the cells. Taking silicon PV cells as an example, although the theoretical limit of photoelectric conversion efficiency can reach approximately 25% , the real conversion efficiency for standard industrial cells falls within the range of 15 to 18% [7]. This means that PV cells convert only a fraction of the absorbed irradiance into electrical energy, with the remainder being

transformed into heat energy and wasted. This excess heat cannot be fully dissipated, increasing the PV cells' temperature. Such underutilized heat not only reduces modules' operational efficiency but also poses a threat to the structural integrity of the PV modules through gradual wear and tear. Research [8] has shown that crystalline silicon PV modules experience a reduction in power output of about 15% with a 20 °C rise in temperature. During hot summer days, the surface of solar panels can reach a temperature of around 66 °C or even higher. Therefore, it's critical to devise a strategy that captures this abundant solar thermal energy to boost the efficiency of PV power production while protecting PV modules from damage [9]. In this work, an effective solution is employed to combine PV and TEG systems as a hybridized system, commonly referred to as a hybrid PV-TEG system. This combined system optimally facilitates the use of extra heat, both the residual waste heat derived from solar radiation and the part generated by PV cells [10]. The collaborative interaction within this hybrid structure not only boosts power generation efficiency but also strengthens the operational reliability of PV modules through the integration of a cooling mechanism provided by TEG modules [11]. TEG modules, operating on the Seebeck effect, i.e., the temperature differential between two distinct metals or semiconductors, can convert thermal energy into electrical energy. This ability positions them as an ideal solution for electricity generation from excess heat [13]. Thus far, a couple of hybrid PV-TEG configurations have been proposed [14], indicating an increase in overall power output ranging from 3% to 16% over traditional PV systems. Therefore, integrating TEG modules with PV modules in this manner not only elevates the performance of the PV system but also capitalizes on the available waste heat, thus boosting overall power output [15].

Researchers primarily utilize the method of directly affixing TEG modules underneath PV panels to construct a hybrid PV-TEG system [16]. Before delving into the electrical dynamics and the interplay between PV and TEG modules, it's crucial to define the thermal interaction model. A detailed analysis of the connections between the operating temperature of PV components and their output efficiency is presented in literature [17]. This examination confirms how the temperature of PV cells/modules is influenced by key climatic factors such as solar irradiance, wind speed, and ambient temperature, whose insights are also applied in this work to illustrate the thermal energy transfer from PV to TEG modules. However, it is pivotal to acknowledge that the environmental conditions during actual operations fluctuate dynamically. Obstructions such as verdant trees, physical structures, and transient clouds invariably cause partial shading conditions (PSCs) on the PV arrays [18], which is critically linked with an escalation in PV cell temperatures called the hotspot effect. The severe increase in temperature not only reduces the efficiency of energy production but also can cause permanent damage to the PV cells' structure in cases of excessive heat [19]. Meanwhile, the alignment of positioning TEG modules underneath PV panels will further spread the adverse effect of PSCs to TEG modules, leading to uneven temperature distribution across TEG modules, known as non-uniform thermal distribution (NTD) [20]. As PSCs give rise to multiple local maximum power points (LMPPs) on the power-voltage (*P-V*) curves of PV cells, NTD similarly induces LMPPs on the power-temperature (*P-T*) curves of TEG modules [21]. In this context, the exploitation of a robust and reliable maximum power point tracking (MPPT) technology to search for the optimal global maximum power point (GMPP) is challenging but also critical for optimizing the system's output power, especially in a dynamic environment with irradiation or temperature variations [22].

To optimize power harvesting by adjusting the operation point under variable operating conditions, particularly in the presence of multiple LMPPs under the PSC and NTD, various MPPT strategies have been devised for both standalone PV/TEG systems and integrated PV-TEG systems [9]. These strategies

fall into two broad groups: conventional methods and intelligence-based approaches. Regarding traditional MPPT techniques that are designed based on only one LMMP, such as perturb and observe (P&O) [24] and incremental conductance (INC) [25], they are struggling to jump out of the complexity of multiple LMPPs, resulting in low-energy harvesting. Thus, more advanced approaches are needed. Model-free meta-heuristic algorithms are highly effective at reducing the complexity of solutions and boosting their self-learning capabilities, making them ideally suited for addressing the aforementioned challenges. For instance, in references [26] and [27], horse herd optimization and improved moth flame optimization are designed to extract optimal power of PV and TEG systems under rapidly changing climatic conditions, respectively. Literature [28] combines grey wolf optimizer (GWO) with cuckoo search (CS) to improve steady-state oscillations and conversion time, thus boosting the MPPT performance. To outline a comprehensive review, reference [29] summarizes the performance, applications, merits, and shortcomings of existing MPPT algorithms in PV systems. Additionally, innovative strategies like dynamical surrogate model-based optimization have been proposed for TEG system output optimization [30], employing a greedy search to promote convergence and efficiently manage heterogeneous temperature variations. Regarding the MPPT for hybrid PV-TEG systems, there are only a few studies proposed to solve this problem, but some noteworthy contributions are achieved, including the application of an arithmetic optimization algorithm (AOA) for optimal power management under dynamic conditions [31] and the use of atomic orbital search optimization (AOS) for stable MPPT performance [32]. In particular, literature [33] incorporates salp swarm algorithm (SSA) into MPPT designs, showing promising results and proving its effectiveness against a variety of established algorithms.

Nevertheless, the investigation on optimal power harvesting of hybrid PV-TEG systems is still in its initial stage and lacks in-depth research and comprehensive discussion. Considering prior studies in this field, three main aspects need to be improved. First, existing studies on MPPT of PV-TEG systems are limited to analyzing technical performance, such as the enhanced power output after MPPT, while overlooking the crucial aspects of sustainability and environmental feasibility, especially the lack of analysis and discussion on carbon emissions. This oversight is significant because the motivation behind the development of green energy technologies, like PV and hybrid PV-TEG systems, is rooted in their potential to reduce carbon emissions, making it an essential criterion for evaluation. This substantial gap in the literature hinders the in-depth investigation of the ecological benefits of these technologies and fails to adequately evaluate their potential as sustainable energy solutions. Second, the lack of diversity in operational scenarios and the absence of real-world data for testing in current research constrain the practical applicability of MPPT methods for PV-TEG systems. The utilization of real-world data is crucial for bridging the gap between theoretical models and practical implementation. Finally, although several MPPT methods are currently proposed for PV-TEG systems and some results have been achieved, there is still a lot of room and necessity for further improvements in maximizing power extraction under different PSCs. Specifically, developing more efficient MPPT strategies for PV-TEG systems can further mitigate the adverse impacts of PSCs on system performance, thereby improving the reliability and economic feasibility of PV-TEG system operations.

To fill up these gaps, this work develops a powerful MPPT technique to harvest the optimal energy output of hybrid PV-TEG systems under PSCs. Meanwhile, a more comprehensive validation and discussion framework regarding MPPT application in hybrid PV-TEG systems is employed, whose main contributions are outlined as follows:

- To boost the conversion rate of captured solar energy, realize the cyclic utilization of waste heat,

boost output energy density, and prolong the service life of PV modules, a PV-TEG hybrid system is devised to combine the benefits of both individual systems;

- For an efficient MPPT performance, a chaotic rime optimization algorithm (c-RIME) based MPPT strategy is developed for the proposed PV-TEG hybrid system to realize optimal energy extraction under diverse operational scenarios, which can further improve the MPPT performance in global convergence rate and extracted energy compared with existing studies;
- Four case studies involving various temperature and irradiance patterns are employed to simulate diverse operational scenarios. Meanwhile, on-site measured datasets collected from four typical days in four different seasons in Hong Kong are applied to verify the applicability of the devised MPPT scheme in real-world settings, offering a comprehensive and realistic assessment. Simulation results indicate that the proposed MPPT strategy for PV-TEG systems outperforms existing studies in output energy;
- A more balanced evaluation framework that equally prioritizes technical advancements and environmental considerations is proposed for the first time to bridge the identified research gap in prior work, which involves real-world datasets and benchmark categories for electricity generation to evaluate carbon emission reduction benefits. This holds significant real-world relevance as it would contribute valuable insights into the optimization of these systems not just for maximum energy output but also for minimal environmental impact like carbon emissions, thus truly reflecting the dual objectives of renewable energy technologies: energy efficiency and environmental sustainability.

The remaining of this work is outlined as: Section 2 introduces the modeling of PV, TEG, and hybrid PV-TEG systems. In Section 3, the MPPT methodology design and implementation framework are elaborated. Section 4 carries out case studies under four testing scenarios. In Section 5, a comprehensive techno-environmental assessment regarding the results is undertaken. Section 6 outlines the main contributions and some future outlooks.

2. Mathematical Modelling

Thus far, the configuration of the hybrid PV-TEG system has been studied by worldwide scholars and engineers using different methodologies, such as thermodynamic methodology. For instance, literature [12] involves a theoretical exploration of the hybrid system using diverse analytical approaches. Literature [34] allocates PV and TEG systems in parallel with the concurrent architectural development of two MPPT controllers aiming to elevate the efficiency of energy harvesting. Additionally, reference [35] provides a comprehensive review of various integration techniques for hybrid systems, accompanied by experimental and numerical analyses aimed at augmenting the output of PV-TEG hybrid configurations.

2.1 PV modeling

Theoretically, an ideal PV cell generates current through the photovoltaic effect occurring at P-N semiconductor junctions, with its equivalent circuit model featuring a source of photogenerated current, diodes arranged in parallel, and resistances in both parallel and series configurations [36]. For practical use, PV modules are configured in series or parallel arrangements as PV arrays to fulfill specific power and voltage requirements [37]. As investigated in literature [21], the dynamics of the output current and voltage of a PV array are related as

$$I_{\mathrm{PV}} = N_{\mathrm{p}} I_{\mathrm{b}} - N_{\mathrm{p}} I_{\mathrm{s}} (\exp[\frac{q}{AKT_{\mathrm{ca}}} (\frac{V_{\mathrm{PV}}}{N_{\mathrm{s}}} + \frac{R_{\mathrm{S}} I_{\mathrm{PV}}}{N_{\mathrm{p}}})] - 1) \quad (1)$$

where the definition of all variables can be referred to Nomenclature.

However, in real-world scenarios, partial shading on PV systems, caused by fluctuating weather or obstructions, not only diminishes their power output but can also cause permanent damage to the modules in extreme cases. Once the PV module or array is shaded, the solar radiation received by the shaded part will be reduced, and correspondingly, the output power generated by the shaded part will be decreased. The shaded PV cells will serve as energy-consuming devices to consume the excess energy generated by other unshaded solar cell strings, leading to decreased energy conversion efficiency. Long-term shadowing on PV components can lead to hotspot effects, which can not only affect the performance of the individual cell but can also damage the entire solar panel component. To avoid this unfavorable result, bypass diodes are usually anti-parallel connected to both ends of the cell string [38]. When a cell group is connected in parallel with a bypass diode and encounters a cell malfunction, the entire circuit's current is determined by the cell with the least current, which is influenced by the shaded area of the cell. If the reverse bias voltage across the malfunctioning cell surpasses its minimum threshold, the bypass diode activates, effectively short-circuiting the malfunctioning cell, as shown in Fig. 1 (a). When the cells are working normally, the bypass diode cuts off in reverse and does not affect the circuit, as shown in Fig. 1 (b). However, the introduction of bypass diodes also leads to multi-peak characteristics in the *P-V* curve of PV arrays under PSCs. The incidence of LMPPs is directly proportional to the number of partially shaded cells, as delineated in Figs. 1 (c) and (d). Additionally, the voltage of a shaded PV cell operates within a set of predefined boundaries, which can be described as follows [10]:

$$V_{\mathrm{reverse}} = nV_{\mathrm{oc}} + V_{\mathrm{Bdiode}} \quad (2)$$

where V_{oc} represents the open circuit voltage, while n signifies the number of PV cells that are exposed without shielding. Additionally, V_{Bdiode} is the variable indicating the voltage drop across the diode.

Currently, the topology configurations commonly utilized for PV arrays include series-parallel (SP) and total-cross-tied (TCT) arrangements [38,39]. The TCT connection, in particular, is noted for its efficiency in minimizing power loss when faced with PSCs, making it a preferred and widely researched connection structure for PV power generation applications.

2.2 TEG modeling

A TEG module operates through the assembly of thermoelectric units that incorporate both P-type and N-type semiconductors, with high and low temperatures at opposite ends to generate electricity based on the Seebeck effect [40]. Figure 2 offers a schematic of a TEG module, in which the mathematical relationship between voltage output and the temperature differential across the module is described by

$$V_{\mathrm{oc}} = \alpha \Delta T = \alpha (T_{\mathrm{h}} - T_{\mathrm{c}}) \quad (3)$$

where T_{h} and T_{c} indicate TEG's hot and cold ends temperature, respectively, and α denotes the Seebeck coefficient.

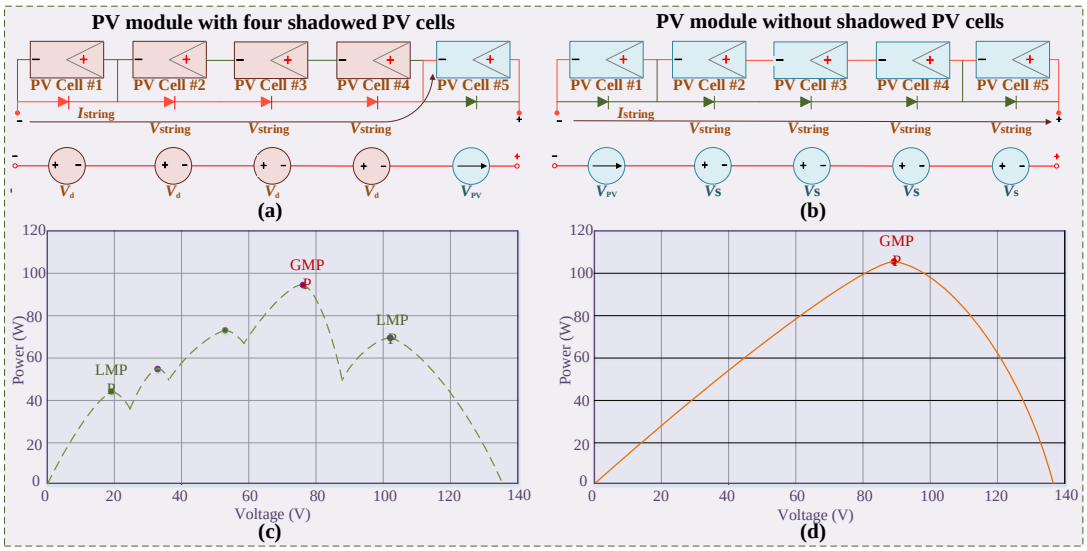

Fig. 1. Output characteristics of PV modules under PSCs. (a) with shaded PV cells, (b) without shaded PV cells, (c) *P-V* output curve under PSCs, and (d) *P-V* output curve without PSCs.

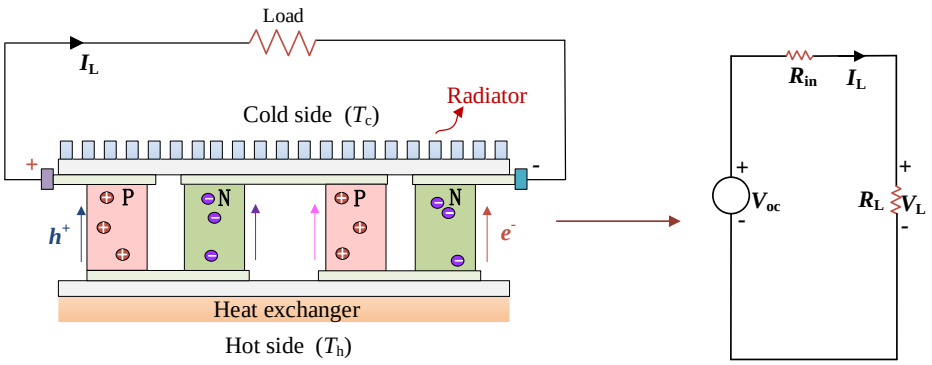

Fig. 2. Schematic diagram of a TEG module.

To accurately model TEG characteristics, a non-zero Thomson coefficient is employed here, as demonstrated in Eq. (4), yields

$$\alpha(T_{\mathrm{av}}) = \alpha_0 + \alpha_1\left(\frac{T_{\mathrm{av}}}{T_0}\right) \tag{4}$$

where α_0 and α_1 are denoted by the essential component and variation rate of Seebeck coefficient, setting as (210 μV/K) and (120 μV/K), respectively, while the other variables can be referred to Nomenclature.

Further, for a typical TEG module, its output power is described by [13]

$$P_{\mathrm{TEG}} = (\alpha\Delta T)^2 \cdot \frac{R_{\mathrm{L}}}{(R_{\mathrm{L}}+R_{\mathrm{TEG}})^2} \tag{5}$$

where all the variables can be referred to Nomenclature.

Achieving optimal power output in a TEG system typically involves arranging multiple TEG modules in various configurations within an array. Unlike PV cells, which act as current sources, TEG units are considered voltage sources. To enhance their output in terms of both current and power, TEG modules are strategically interconnected in series or parallel formations, a practice referred to as SP topology. This method not only facilitates efficient power generation but also allows for the refinement and optimization of power production [13]:

$$I_i = \begin{cases} (V_{oci} - V_{Li}) \cdot \frac{I_{sci}}{V_{oci}} = I_{sci} - \frac{V_{Li}}{R_{TEGi}}, \text{if } 0 \le V_{Li} \le \frac{I_{sci}}{V_{oci}}, i = 1,2,\dots,N \\ 0, \text{otherwise} \end{cases} \quad (6)$$

where all the aforementioned variables are specified in Nomenclature.

The power output from an individual TEG unit i is expressed by

$$P_{TEGi} = \begin{cases} V_{Lii} \cdot I_i = I_{sci} V_{Li} - \frac{I_{SCi}}{R_{TEGi}} V_{Li}^2, \text{if } 0 \le V_{Li} \le \frac{I_{sci}}{V_{oci}}, i = 1,2,\dots,N \\ 0, \text{otherwise} \end{cases} \quad (7)$$

where P_{TEGi} represents the power output from the ith TEG module.

The overall power produced by a TEG array, which is essentially the aggregate of the power outputs of each module within the array, can be expressed as follows:

$$P_{TEG\Sigma} = \sum_{i=1}^{N} P_{TEGi} \quad (8)$$

2.3 Hybrid PV-TEG system modelling

Since PV and TEG modules are physically integrated, the thermal interaction between PV and TEG modules is directly transferred via their physical connection, as shown in Fig. 3.

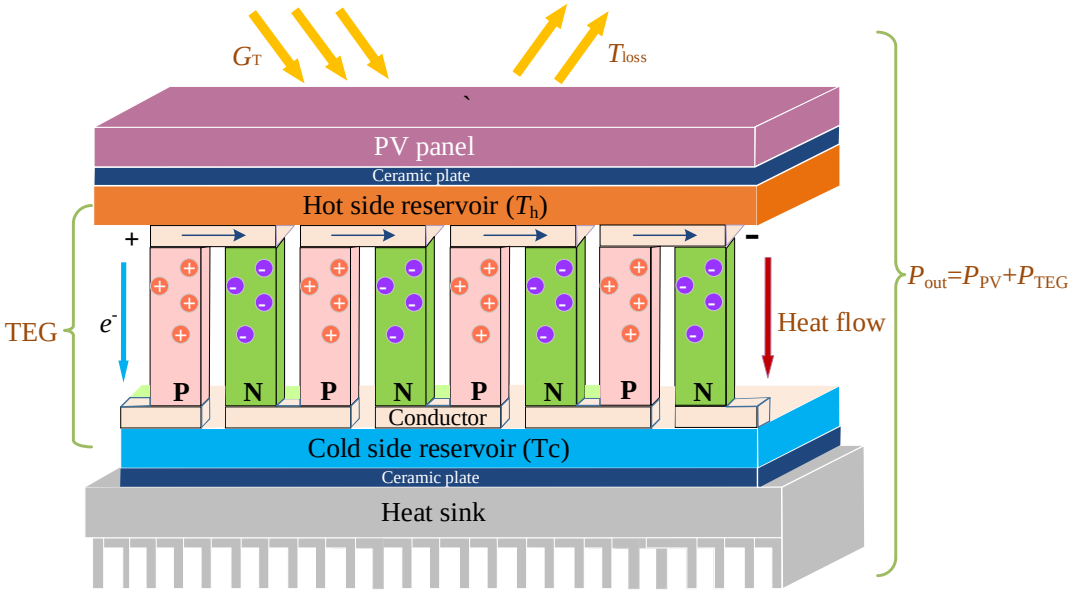

Fig. 3. Integration structure of a hybrid PV-TEG module.

In the practice and exploration of actual engineering applications, although the SP connection has achieved a wide range of applications but shows obvious limitations when applied to the array layout of PV power generation, especially under PSCs. In contrast, TEG arrays based on this SP connection mode still maintain adaptability and suitability under NTD. Therefore, in this work, PV arrays and TEG arrays respectively employ TCT and SP connection pattern, as shown in Fig. 4.

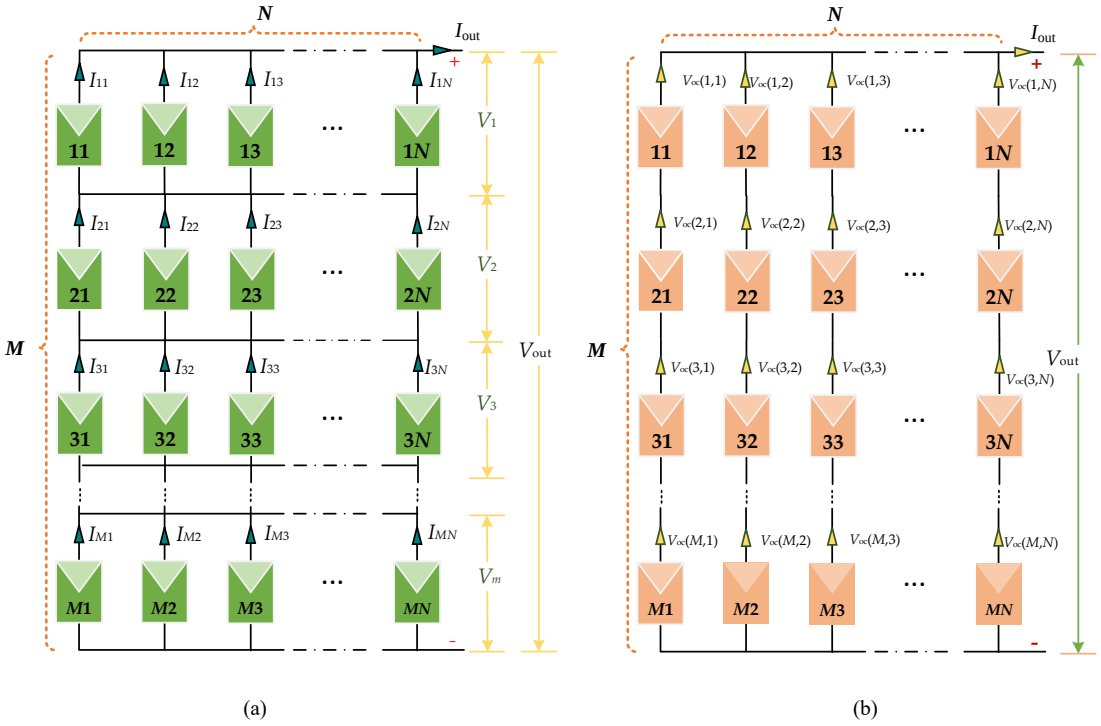

Fig. 4. Configurations of PV and TEG arrays. (a) TCT connection structure of PV array with ($M\times N$) modules and (b) SP connection structure of TEG array with ($M\times N$) modules.

Moreover, dual MPPT controllers and boosting circuits are respectively employed for PV and TEG systems for power aggregation, as illustrated in Fig. 5.

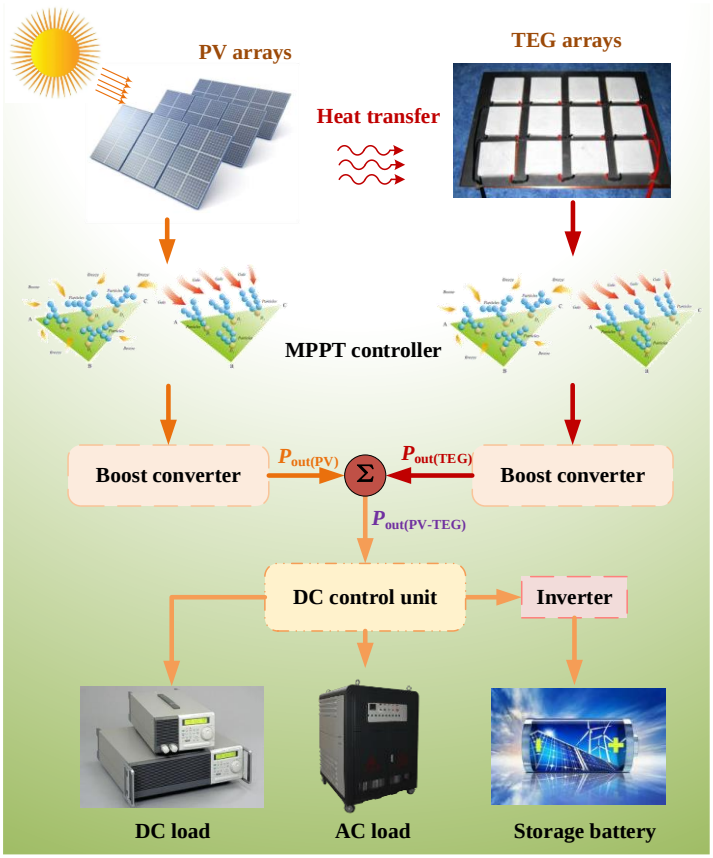

Fig. 5. Schematic of MPPT structure for hybrid PV-TEG system.

Based on this hybrid energy generation pattern, the waste heat produced by PV systems can be sufficiently re-utilized by TEG modules while TEG systems also, in turn, enhance PV power production efficiency by providing a passive cooling mechanism to lower the operational temperature of PV modules. This synergistic relationship, as elaborated in reference [17], is defined through a heat transfer equation, which calculates the temperature of the TEG module's hot side using variables such as ambient temperature (T_{am}), wind speed (W_s), and the intensity of solar irradiance (G_T), as follows [17]:

$$T_{op} = 0.943T_{am} + 0.028G_T - 1.528W_s + 4.3 \quad (9)$$

As shown in Fig. 3, TEG modules are directly configured with their hot sides attached beneath PV modules, and their cold side's temperature equals T_{am}.

The overall power generation of this combined system is presented as

$$P_{PV-TEG} = P_{PV} + P_{TEG} \quad (10)$$

Moreover, the efficiency of converting power within the PV-TEG hybrid setup is directly linked to the operational efficiencies of the individual PV and TEG units, as follows [29]:

$$\eta_{pv-teg} = \frac{P_{PV}+P_{TEG}}{G_T \times S_{PV}} \quad (11)$$

where S_{PV} denotes the PV board area.

3. Methodology and MPPT design

This section introduces the optimization principles of the proposed c-RIME and its relevant MPPT design for the hybrid PV-TEG system.

3.1 Rime optimization algorithm

RIME optimization algorithm draws inspiration from the natural phenomenon of rime ice formation [41], which is influenced by specific environmental parameters including temperature, wind speed, and humidity levels. The algorithm mimics the formation patterns of rime ice, categorized into soft and hard rime based on wind conditions. Soft rime grows slowly under light wind conditions with changing wind directions, while hard rime forms quickly under strong wind conditions with consistent wind direction. RIME algorithm integrates these growth behaviors into exploitation and exploration strategies, enhancing its performance in solving optimization problems. For an explicit illustration, the specific soft rime and hard rime formation based searching movements are illustrated in Fig. 6 (a) and (b), respectively.

RIME optimization algorithm draws inspiration from the natural process of rime ice formation, which is influenced by specific environmental parameters including temperature, wind speed, and humidity levels. Mimicking the formation patterns of rime ice, categorized into soft and hard rime based on wind conditions, the algorithm adopts this biological principle to enhance computational and system optimization strategies.

3.1.1 Rime population initialization

Drawing inspiration from natural processes, each rime represents as an exploratory agent within the algorithm and the group of all such agents is considered the algorithm's population. Initially, the entire rime population, denoted as R is established, which is comprised of n distinct rime agents, symbolized

as A_i, where each agent further consists of d rime-particles, indicated as x_{ij}. Consequently, the population of rime agents R is mathematically characterized by the rime-particles x_{ij}, defined by [41]

$$R = \begin{bmatrix} A_1 \\ A_2 \\ \vdots \\ A_i \end{bmatrix}; A_i = [x_{i1}, x_{i2}, \cdots, x_{ij}] \tag{12}$$

$$R = \begin{bmatrix} x_{11} & x_{12} & \cdots & x_{1j} \\ x_{21} & x_{22} & \cdots & x_{2j} \\ \vdots & \vdots & \ddots & \vdots \\ x_{i1} & x_{i2} & \cdots & x_{ij} \end{bmatrix} \tag{13}$$

3.1.2 Soft rime searching strategy

Under low wind speed conditions, the growth of soft rime is highly unpredictable, causing rime particles to become widely dispersed over the surface, although growing slowly in a uniform direction. This study introduces a soft-rime searching method based on this randomness and broad coverage, allowing it to quickly explore the entire searching region initially and avoid premature convergence to a local optimum. In total of five motions are adopted to simulate particle condensation and calculate the positions of rime particles, as summarized in Fig. 6 (a), and the position of each particle is calculated by Eq. (14), as follows [41]:

$$R_{ij}^{\text{new}} = R_{\text{best},j} + r_1 \cdot \cos\theta \cdot \beta \cdot \left(h \cdot \left(Ub_{ij} - Lb_{ij}\right) + Lb_{ij}\right), r_2 < E \tag{14}$$

where R_{ij}^{new} represents the updated position of particle j within rime-agent i, $R_{\text{best},j}$ corresponds to particle j within the best rime-agent thus far, r_1 means a random factor ranging between -1 and 1 that, together with $\cos\theta$, determines the particle's movement direction and varies with the iterations, as detailed in Eq. (15). The environmental influence β changes with the iteration number to mimic external conditions and ensures the algorithm's convergence, as described in Eq. (16). Finally, the adhesion degree h, denotes a random value between 0 and 1.

$$\theta = \pi \cdot \frac{t}{10 \cdot T} \tag{15}$$

$$\beta = 1 - \left[\frac{w \cdot t}{T}\right] / w \tag{16}$$

$$E = \sqrt{(t/T)} \tag{17}$$

where t and T denote the current and maximum iteration number, respectively, and w is set as 5.

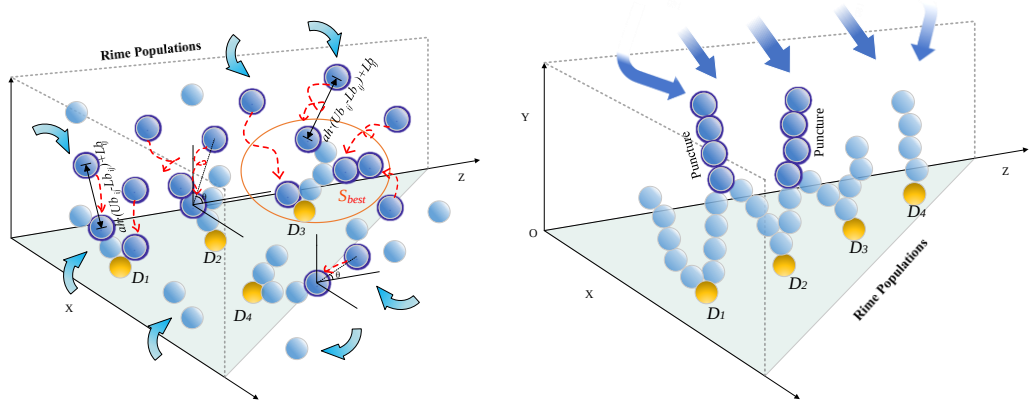

(a) (b)

Fig. 6. Schematic of rime searching movements. (a) soft rime searching and (b) hard rime puncturing.

3.1.3 Hard rime puncture mechanism

In the context of intense wind conditions, hard rime develops in a straightforward, consistent manner. Inspired by this puncturing behavior, a hard-rime puncture pattern is designed to refine the algorithm's effectiveness. This allows for the exchange of particles between agents, a critical feature designed to improve the algorithm's ability to converge towards optimal solutions and avoid local optimums effectively. The puncturing process is illustrated in Fig. 6 (b), with the particle exchange described in Eq. (18), as follows [41]:

$$R_{ij}^{\text{new}} = R_{\text{best},j}, \quad r_3 < F^{\text{normr}}(S_i) \tag{18}$$

where F^{normr} signifies the normalized fitness value of current agent and r_3 denotes a random number within the range of (-1, 1).

3.1.4 Positive greedy selection mechanism

To further augment the algorithm's capacity for global search, an advanced greedy selection method is introduced. This involves comparing the fitness value of an agent post-update with its pre-update value. If the new value shows improvement, both the fitness value and the agent's solution are updated. This not only ensures the continuous presence of high-quality agents within the population, enhancing the overall solution quality but also introduces significant changes in agent positions across iterations. Such dynamic changes can lead to some agents performing worse than before the update, potentially hindering progress in subsequent iterations. However, this mechanism is designed to steer the population towards more optimal outcomes with each iteration, ensuring a more effective evolutionary process.

Overall, the execution framework for RIME is tabulated in Table 1.

Table 1. Pseudo-code of RIME for solving optimization problems

Initialization of rime population R
Determine the best agent at the current iteration and its fitness value
While $t \leq T$
Determine the coefficient of adherence E via Eq. (17)
If $r_2 < E$
Update rime positions employing soft-rime searching via Eq. (14)
End If
If r_3 >Normalize fitness of S_i
Undertake hard-rime puncturing operation via Eq. (18)
End If
If $F(R_i^{\text{new}}) < F(R_i)$
Solution evaluation and update based on positive greedy selection
End If
$t = t+1$
End while

Chaotic rime optimization algorithm

The initialization of a population algorithm significantly influences its subsequent searching efficiency. In the absence of prior information, initial solutions in RIME are often generated through random initialization, resulting in an uneven distribution of individuals within the initial population. This uneven distribution can lead to reduced diversity and lower quality of population, consequently affecting the convergence process. Chaos mapping [42], characterized by randomness and sensitivity, can simultaneously improve the solution diversity and contribute to jumping out of the local optimums. Commonly used chaos mappings include Logistic mapping, Tent mapping, and Circle chaos mapping. Among these, Circle mapping is noted for its stability and high coverage of chaotic values. However, considering that the Circle mapping has a denser value distribution between 0.2 and 0.6, leading to an uneven distribution, improvements to the Circle mapping formula have been proposed to achieve a more uniform distribution. The original expression for Circle chaos mapping is [43]:

$$x_{n+1} = \mathrm{mod}(x_n + 0.2 - \frac{0.5}{2\pi}\sin(2\pi x_n),1) \tag{19}$$

$$x_{n+1} = \mathrm{mod}(x_n + 0.2 - \frac{0.5}{2\pi}\sin(2\pi x_n),1) \tag{20}$$

The expression for the improved Circle chaos mapping is as follows:

$$x_{n+1} = \mathrm{mod}(3.85x_n + 0.4 - \frac{0.7}{3.85\pi}\sin(3.85\pi x_n),1) \tag{21}$$

where *n* represents the dimension of the solution.

Figure 7 illustrates an explicit comparison of the improved Circle mapping for initialization with Tent chaos mapping and Logistic chaos mapping. The results show that the Logistic mapping has a relatively uniform probability distribution in the middle range, but probabilities are significantly higher at both ends. This characteristic is disadvantageous for locating the global optimum when it does not reside at the extremes of the design variable space. Secondly, although the Tent mapping exhibits relatively good ergodicity, its iteration sequences contain short cycles and unstable periodic points, leading to potential stability in the sequences and algorithm failure. Lastly, the improved Circle mapping is more stable and exhibits better uniformity in distribution. Therefore, this work employs the improved Circle mapping to initialize the RIME population, aiming to enhance and improve the initial population's distribution quality in the search space, thereby strengthening its global searching capability.

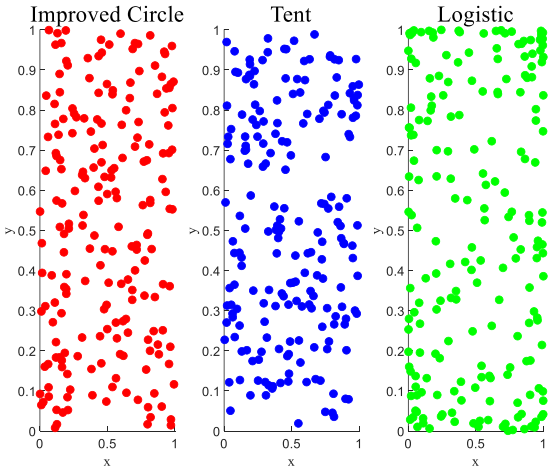

Fig. 7. Population initialization distribution of three chaos mapping methods.

3.2 MPPT design for PV-TEG system under PSC

3.2.1 Objective function design

According to the practical operational requirements, the voltage outputs derived from both PV and TEG systems are considered as adjustable variables open to optimization. The fitness function at each control iteration can be precisely articulated by real-world voltage and current data, as follows:

$$\min f(V_{\mathrm{PV}}) = -P_{\mathrm{out}}(V_{\mathrm{PV}}) = -V_{\mathrm{PV}} * I_{\mathrm{PV}}(V_{\mathrm{PV}}) \tag{22}$$

$$\text{s. t. } V_{\mathrm{PV}}^{\min} \le V_{\mathrm{PV}} \le V_{\mathrm{PV}}^{\max} \tag{23}$$

where P_{out} represents the power produced by PV system. Simultaneously, $V_{\mathrm{PV}}^{\min}$ and $V_{\mathrm{PV}}^{\max}$ denote the minimal and maximal constraints of its output voltage, defining the boundary conditions within which the output voltage operates.

The establishment of the fitness function for TEG systems resembles the approach employed for PV systems, as outlined below

$$\min f(V_{\mathrm{TEG}}) = -P_{\mathrm{out}}(V_{\mathrm{TEG}}) = -V_{\mathrm{TEG}} * I_{\mathrm{TEG}}(V_{\mathrm{TEG}}) \tag{24}$$

$$\text{s. t. } V_{\mathrm{TEG}}^{\min} \le V_{\mathrm{TEG}} \le V_{\mathrm{TEG}}^{\max} \tag{25}$$

where P_{out} indicates the power generated by TEG system, $V_{\mathrm{TEG}}^{\min}$ and $V_{\mathrm{TEG}}^{\max}$ indicate the minimal and maximal constraints of TEG system's output voltage, defining the allowable operational range for power output.

3.2.2 Boost converter model

To implement MPPT control to optimize the power output, the essential execution basis is by adjusting the power converter's duty cycle. By fine-tuning the duty ratio, MPPT techniques seek to identify the optimal operating point that yields the highest power output. The boost circuit is often characterized as a non-isolated DC-DC converter designed to increase the voltage from its input power source to a desired level [44]. For a more intuitive demonstration, Fig. 8 shows how the proposed c-RIME based MPPT algorithm and boost converter work together to optimize energy conversion in a PV-TEG hybrid system under PSCs.

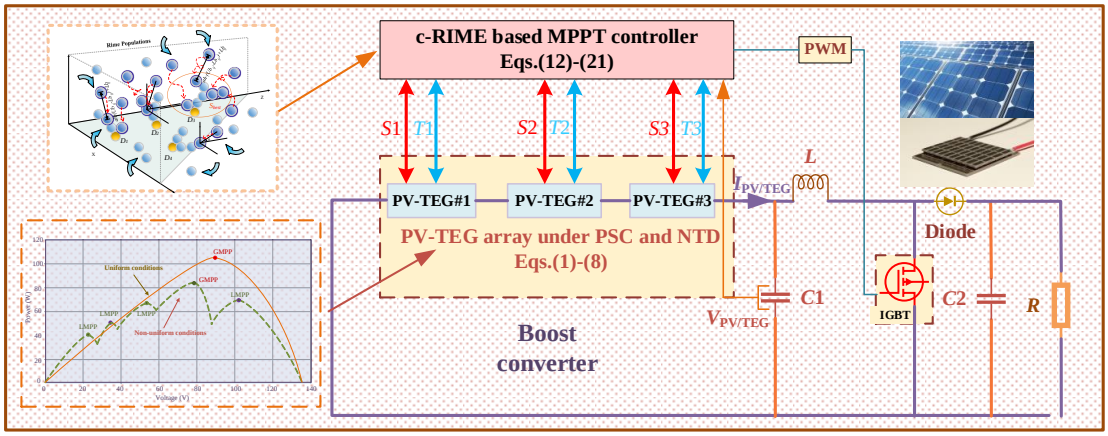

Fig. 8. c-RIME based MPPT controller for hybrid PV-TEG system under PSCs.

In Fig. 8, $V_{\text{PV-TEG}}$ indicates the output voltage from this configuration. Meanwhile, V_{out} signifies the voltage associated with the improvement of the boost circuit. Further exploration reveals that parameter f denotes the switching frequency related to the IGBT and its subsequent control cycle. I_{L}

and I_{Lmax} are used to represent the standard and maximum currents flowing through inductor L. In detail, V_{out}, the inductor L, and the filter capacitance C_1, are determined as

$$V_{\mathrm{out}} = \frac{V_{\mathrm{PV\text{-}TEG}}}{1-D\mathrm{c}} \tag{26}$$

$$L = \frac{V_{\mathrm{out}}}{4I_{\mathrm{Lmax}} \times f} \tag{27}$$

$$C_1 = L \times \frac{\left(I_{\mathrm{L}}+I_{\mathrm{pmax}}/2\right)^2-\left(I_{\mathrm{L}}-I_{\mathrm{pmax}}/2\right)^2}{(V_{\mathrm{in}}+0.005V_{\mathrm{in}})^2-(V_{\mathrm{in}}-0.005V_{\mathrm{in}})^2} \tag{28}$$

A detailed presentation of parameters associated with the boost circuit, specifically tailored for the dual subsystems present in the PV-TEG hybrid setup, is tabulated in Table 2. Generally, DC-DC converters inherently encounter power dissipation, consequently, the efficiency of tracking associated with MPPT technology can be expressed in the following manner:

$$\eta_{\mathrm{MPPT}} = \frac{P_{\mathrm{PV-TEG}}(t)}{P_{\mathrm{max}}(t)} \times 100 \tag{29}$$

At a specific time point, labeled as t, the hybrid system reaches a particular power output denoted as $P_{\mathrm{PV\text{-}TEG}}(t)$.

Table 2. Critical parameters of boost circuits

Parameter	PV system	TEG system
Capacitor	C_1=C_2=1 μF	C_1=66 μF, C_2=200 μF
Inductor(L)	500 mH	250 mH
Resistive load(R)	200 Ω	10 Ω
Switching frequency	100 kHz	f_s=20 kHz

3.2.3 MPPT implementation procedure

In the realm of integrated PV-TEG setups, MPPT operation seamlessly incorporates distinct techniques inherent to each subsystem. Highlighting the non-model-based MPPT strategy, it relies on the accurate measurement of two essential parameters: voltage and current. Based on the aforementioned introduction, the MPPT implementation procedures of the proposed c-RIME based MPPT control strategy are demonstrated in Fig. 9, which aims to maximize the power output and mitigate the undesirable impacts of PSCs.

4. Case Studies

This section verifies the effectiveness of the proposed c-RIME based MPPT controller for the designed PV-TEG hybrid system under various operational conditions of PSCs and NTD. In detail, four different scenarios are employed, namely, startup test, stepwise solar irradiation variations, random solar irradiation fluctuations, and real-world scenarios based on field atmospheric data collected from Hong Kong. At the same time, to simulate the PSCs and NTD under extreme conditions, the partial shading factors of the three PV-TEG modules are respectively set as 1, 0.6, and 0.3. This design is particularly challenging for random fluctuations in solar irradiation and Hong Kong tests, which heavily rely on the algorithm's global optimization capabilities.

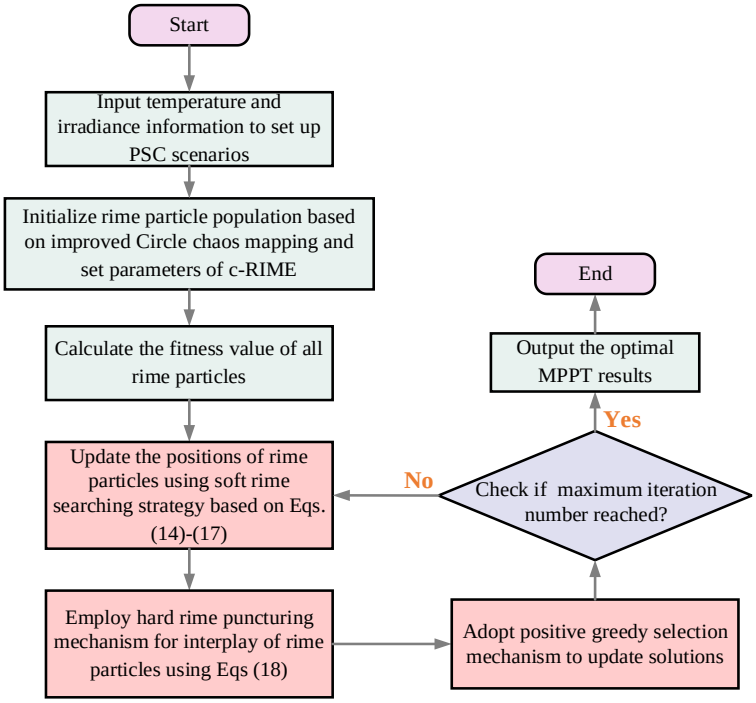

Fig. 9. MPPT implementation framework for hybrid PV-TEG system using c-RIME under PSCs.

For a comprehensive comparative analysis, conventional P&O, and eight additional well-known meta-heuristic algorithms, including reptile search algorithm (RSA) [45], multi-verse optimization (MVO) [46], moth-flame optimization (MFO) [47], sine cosine algorithm (SCA) [48], as well as three algorithms that have been utilized to solve this problem in prior work, i.e., AOA [31], AOS [32], and SSA are employed. To maintain consistency and fairness in the comparison, the population size (N_p) has been identically set as 10, while the maximum iteration number (k_{max}) is designed as 5. Furthermore, for INC and P&O, their step sizes are set as 10^{-7}. Meanwhile, the critical component parameters of the designed PV-TEG hybrid system are tabulated in Table 3.

Table 3. Critical parameters of PV-TEG hybrid system

PV module		**TEG module**	
Type	User-defined	Type	TGM199-1.4-2.0
Typical peak power	213.15 W	Parameter measurement conditions	T_c=30 ℃, T_h=200 ℃
MPP Voltage	29.00 V	Component dimensions	40 mm×40 mm×4.4 mm
MPP current	7.35 A	Typical peak power	7.3 W
Short-circuit current(I_{sc})	7.84 A	I_{sc}	2.65 A
Open-circuit voltage(V_{oc})	36.30 V	V_{oc}	11 V
Temperature coefficient of Isc(k_1)	3 mA/℃	Number of thermoelectric units	200

4.1 Startup test

Startup test aims to assess the capability of MPPT techniques to adapt to uneven solar irradiance across PV arrays, which mimics real-world conditions where shadows from nearby objects or static clouds create non-uniform irradiance distribution. This test simultaneously validates the MPPT algorithm's responsiveness and the stability of its convergence from an initial zero point, focusing on how quickly and reliably the system can reach and maintain the maximum power point during the initial phase under PSCs. To simulate PSCs and NTD on hybrid PV-TEG modules, the solar irradiation levels

for three PV arrays are respectively set at varied intensities: 800W/m^2, 600W/m^2, 700W/m^2, while the ambient temperature is maintained at 25 ℃. Regarding the calculation of hot side input temperature for TEG modules, it can be determined using Eq. (9) with the assumption that the cold side temperatures are consistently maintained at 25 ℃. This setup allows for the analysis of the TEG modules' performance under controlled temperature differences, which is crucial for optimizing energy conversion efficiency. Figure 10 demonstrates the power and energy output obtained by ten various MPPT algorithms under startup test, which indicates that c-RIME outperforms other algorithms in terms of both power and energy output under PSCs and NTD.

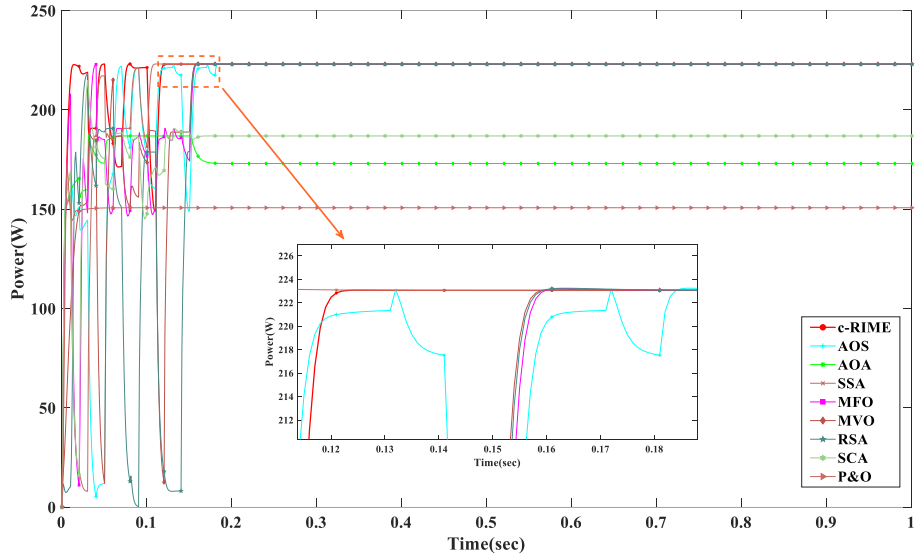

(a)

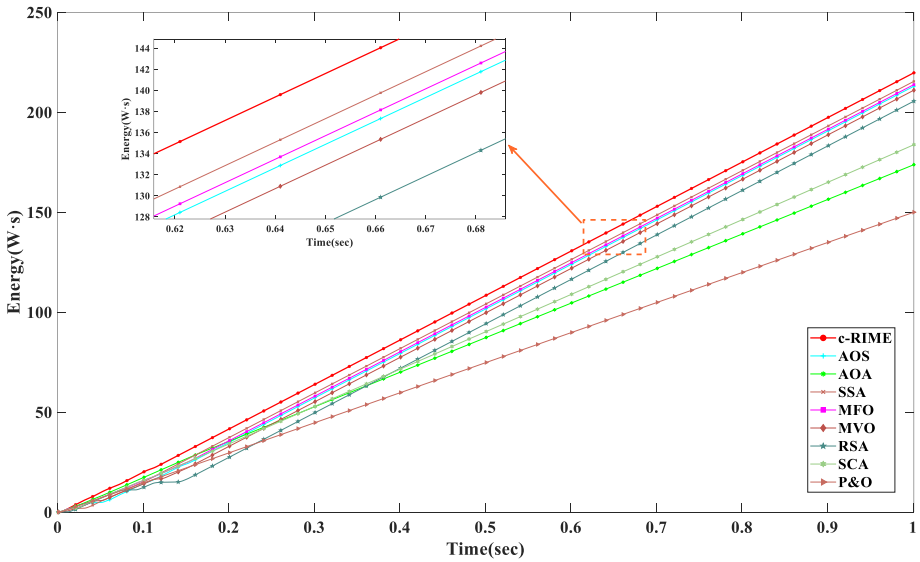

(b)

Fig. 10. Start-up test results of ten MPPT techniques for hybrid PV-TEG system. (a) power output and (b) energy output.

Figure 10(b) indicates that c-RIME reaches a higher energy output level quicker than its competitors, such responsiveness is critical for PV-TEG systems to maximize energy harvest under PSC. Meanwhile, Figure 10(a) suggests a stable convergence of c-RIME to the maximum power point, which is essential for ensuring reliable energy output in fluctuating environmental conditions.

4.2 Stepwise variations in solar irradiation

This section investigates the scenario where clouds move at a high speed while the environmental temperature remains at 25℃, and its influence on the energy output of PV-TEG hybrid modules. From Fig. 11, it can be observed that every individual PV panel witnesses different step changes in solar irradiation, such that the input temperature of each TEG module's hot side is correspondingly calculated and changed according to Eq. (9).

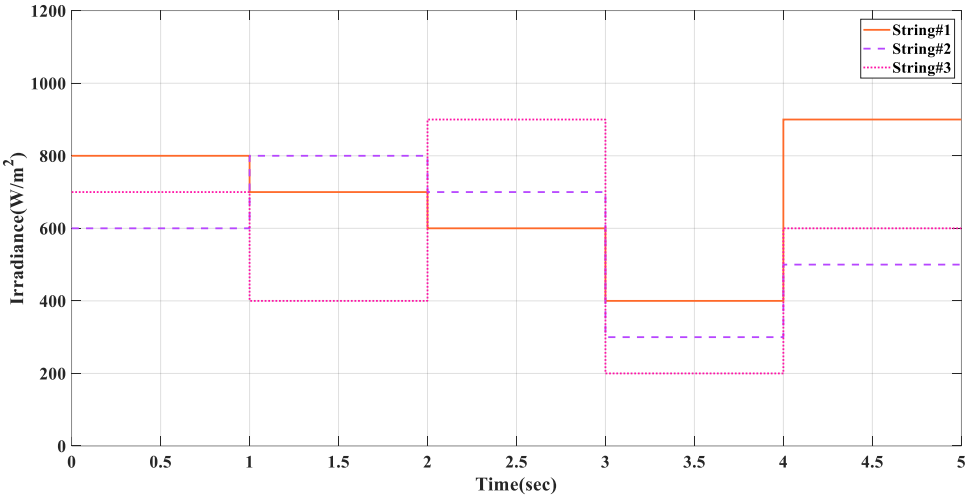

Fig. 11. Step changed solar irradiation under PSCs.

For this case, to ensure the consistency of atmospheric conditions, the W_s persists at a constant 1.5 m/s. Figure 12 depicts the optimal simulation results obtained by different methods under stepwise solar irradiation variations.

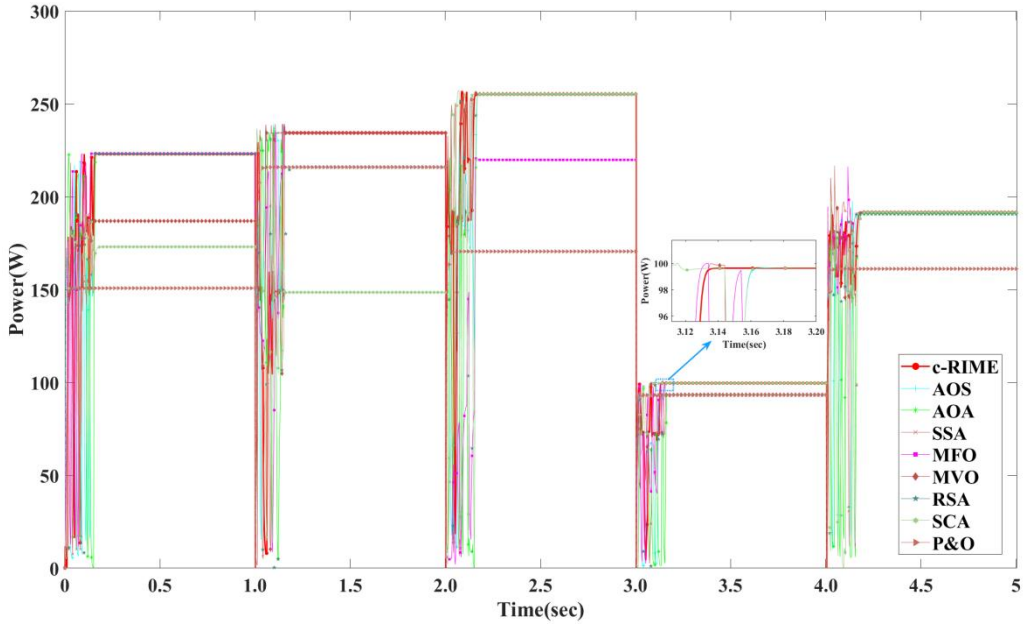

(a)

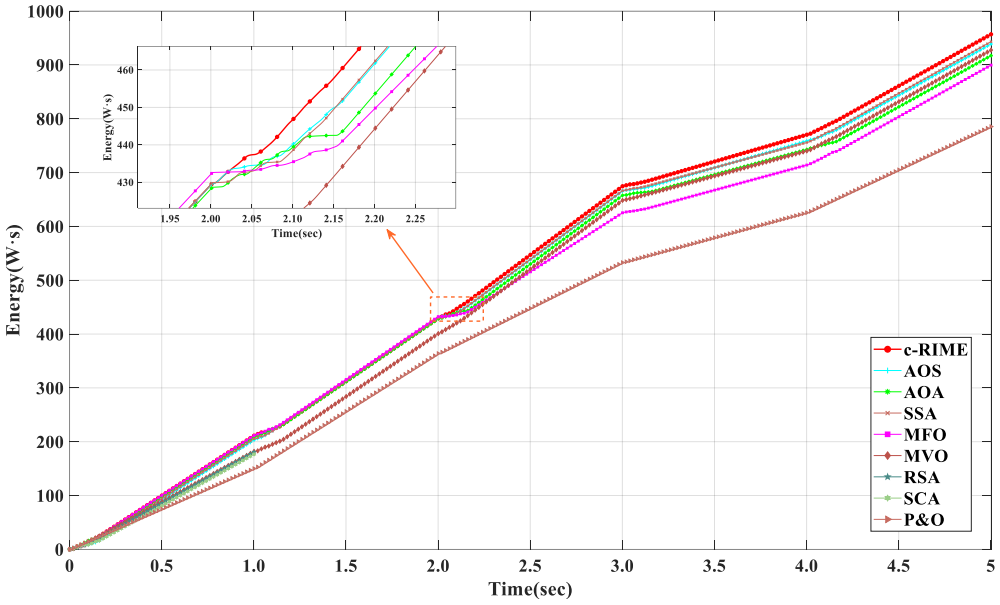

(b)

Fig. 12. Stepwise variations in solar irradiation test results of ten MPPT techniques for hybrid PV-TEG system. (a) power output and (b) energy output.

Figure 12 (b) indicates that c-RIME not only adapts quickly but also maximizes energy output more efficiently than its competitors within the test duration. For instance, during the narrow time window between 1.95 and 2.25 seconds, c-RIME shows a remarkable ability to enhance energy accumulation, which is pivotal during transient weather conditions. Consistent with its energy output superiority, c-RIME also demonstrates outstanding adaptability in power output under stepwise changes in solar irradiance. It can be seen from Fig. 12(a) that c-RIME shows a more pronounced ability to sustain higher power levels immediately and stably following the step changes, which suggests that c-RIME can better maintain optimal operation points and minimize performance drops due to environmental fluctuations.

4.3 Stochastic change in solar irradiation

To more realistically reflect the operating dynamics of PV systems during the peak summer season, where sunlight can cover up to 12 hours, continuous and random fluctuations in irradiance conditions over a 12-hour daylight cycle is employed here, as shown in Fig. 13.

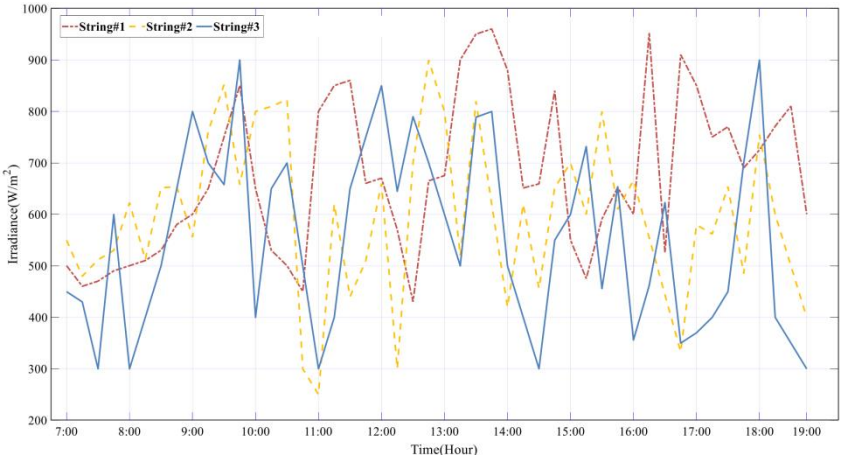

Fig. 13. Stochastic irradiation change of hybrid PV-TEG system.

In this scenario, the hot side of TEG modules undergoes both consistent and random thermal

fluctuations over 12 hours. It is crucial to highlight that, to more accurately mirror actual environmental conditions, the wind speed, denoted as *W*s, is specified within a range spanning 1 to 10 m/s in this case. This simulation provides a rigorous test of the MPPT algorithms' ability to adapt to highly variable and unpredictable environmental conditions. It underscores the importance of algorithm responsiveness, adaptability, and efficiency in managing the unpredictable nature of solar energy availability, thermal fluctuations, and the impact of wind speed on system performance. MPPT outcomes obtained by ten distinct methods are illustrated in Fig. 14.

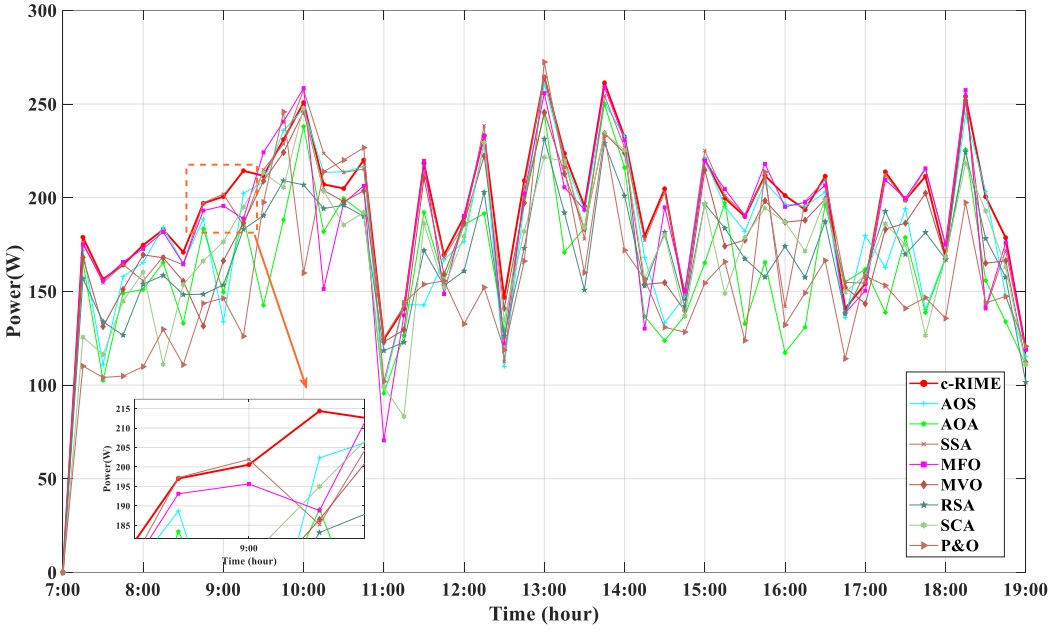

(a)

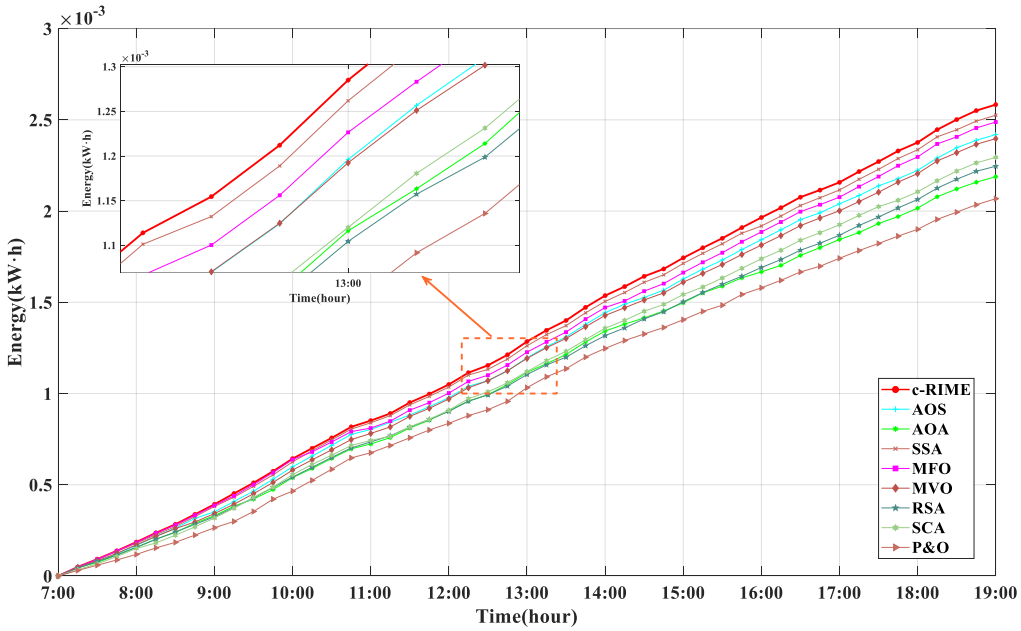

(b)

Fig. 14. Stochastic change in solar irradiation test results of ten MPPT techniques for hybrid PV-TEG system. (a) power output and (b) energy output.

Figure 14 (a) demonstrates that c-RIME shows remarkable adaptability, maintaining higher power

levels compared to other algorithms such as AOS, AOA, SSA, MFO, MVO, RSA, SCA, P&O, and INC, particularly during peak irradiance hours such as time from 13:00 to 15:00. This indicates superior algorithm efficiency in converting available solar energy into electrical power during periods of maximum irradiance. The energy output in Fig. 14 (b) further evidences the superiority of c-RIME algorithm in efficiently accumulating energy over time, outpacing competitors throughout the day. For instance, the detailed energy output during the midday hours (e.g., between 10:00 and 11:00) emphasizes c-RIME's consistent performance even as conditions rapidly change. This highlights the algorithm's robustness and reliability in optimizing energy harvest under stochastic environmental variability.

4.4 Field-measured temperature and solar irradiation data in Hong Kong

In this section, to validate the performance of these MPPT algorithms under real-world conditions, real solar irradiance and temperature datasets collected from four distinct days representing the seasons in Hong Kong in 2022 are utilized, which are recorded at ten-minute intervals. Simulation and theoretical models provide a controlled simulation environment for the feasibility and initial testing of MPPT algorithms. However, incorporating real-world data introduces the complexity and unpredictability of natural conditions, thus providing a robust validation framework. By analyzing algorithm performance with actual temperature and solar irradiation variations, the adaptability and robustness of MPPT algorithms to environmental changes can be more practically assessed. Hong Kong is situated in the southern coastal region of China, characterized by a subtropical climate. This climate type is marked by hot, humid summers and mild, with temperatures frequently ranging from 26 °C to 33 °C. Winters are mild and relatively dry, and temperatures during this season typically range from 10 °C to 20 °C. Due to its geographical location and climatic conditions, Hong Kong experiences significant seasonal variations in solar irradiation and ambient temperatures, making it an ideal case study for evaluating MPPT algorithm performance in real-world operation conditions. Figure 15(a) shows the locations where the data are sampled, at 22.3°N and 114.2°E, respectively. Figure 15(b) demonstrates the specific instruments used for measurements within this study. To mimic PSCs, the solar irradiances of three PV panels are set as 100%, 60%, and 30% of the measured data in Hong Kong to symbolize the long-term, continuous graded changes. In this case, the wind speed W_s is designed within a range of 1-10m/s.

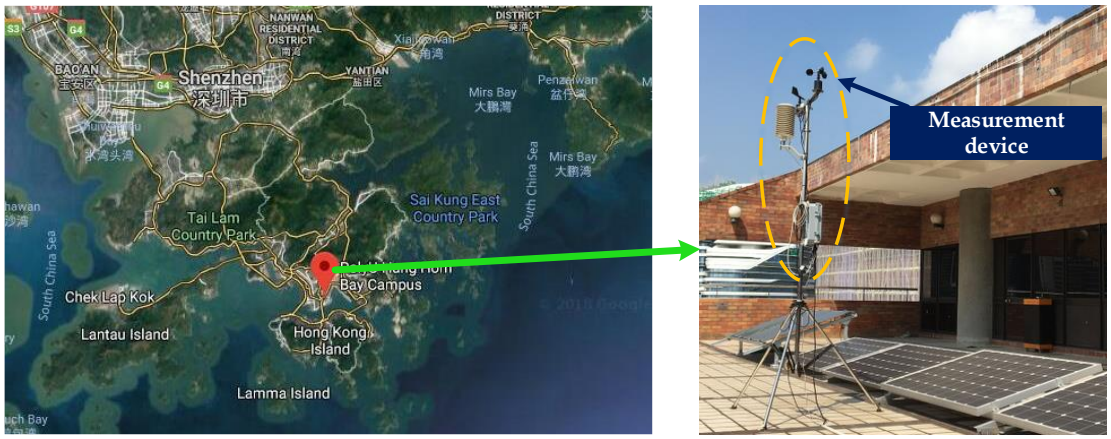

(a) (b)

Fig. 15. Solar radiation and temperature measurement device and its location. (a) measurement location and (b) measurement device.

On-site collected irradiance data is illustrated in Fig. 16 (a), representing four distinct days across the four seasons in Hong Kong, meanwhile, Fig. 16 (b) demonstrates the corresponding changes in

ambient temperature.

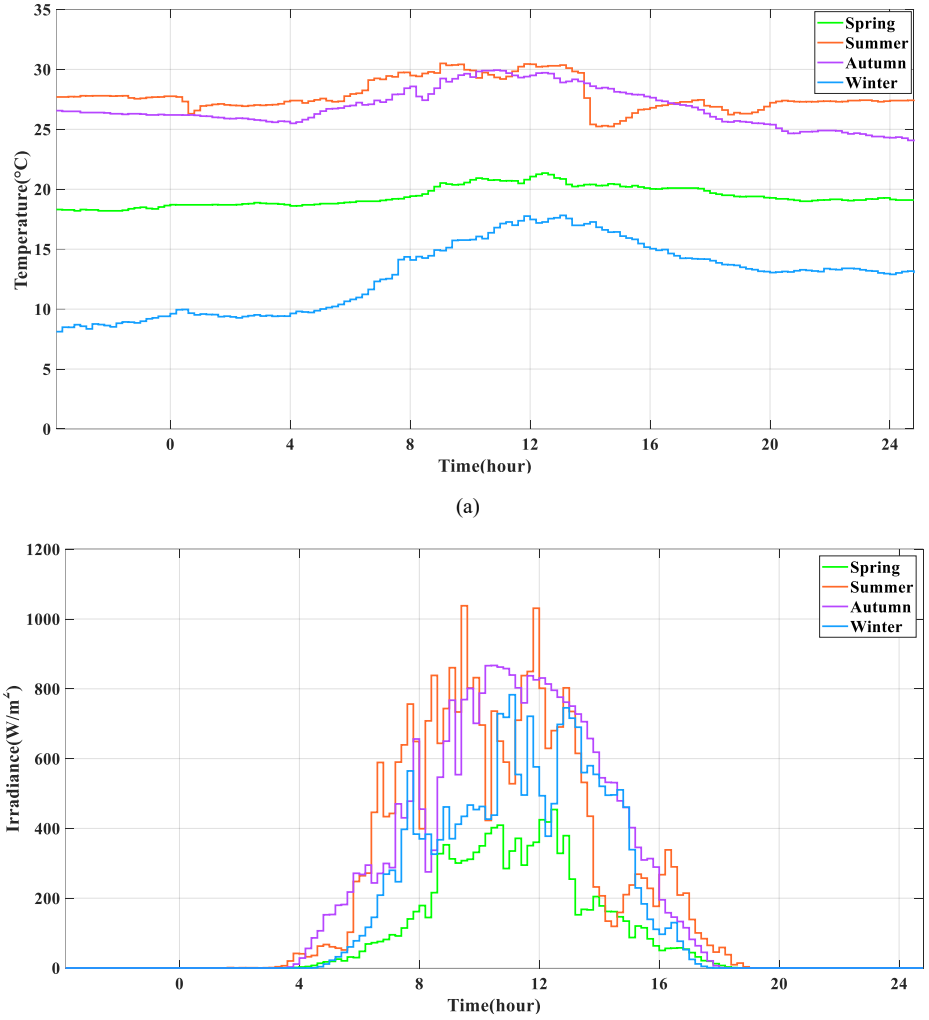

Fig. 16. Temperature and irradiation distribution of four typical days in Hong Kong. (a) Solar irradiation and (b) Temperature.

Figures 17 and 18 show optimal output power and energy obtained by ten methods using on-site measurement data from Hong Kong across four typical days representative of spring, summer, autumn, and winter. Simulation results verify its consistent outperformance across all seasons, suggesting that c-RIME is highly adaptable, efficient, and reliable regardless of the seasonal variability in solar irradiance and temperature. For instance, in spring, the power output for all MPPT techniques appears relatively moderate, where c-RIME algorithm, however, demonstrates a slightly higher power output compared to other algorithms, indicating its efficient adaptability to the mild and variable spring conditions in Hong Kong. The summer data shows a significant increase in power output for all techniques, which corresponds with the higher solar irradiance levels characteristic of Hong Kong's summers. Again, c-RIME algorithm stands out, achieving the highest power output among the techniques tested. Regarding the energy output in Fig. 18, across all seasons, c-RIME consistently achieves the highest energy output, underscoring its adaptability and efficiency in a wide range of environmental conditions, which highlights the algorithm's superior optimization capabilities for maximizing energy harvest.

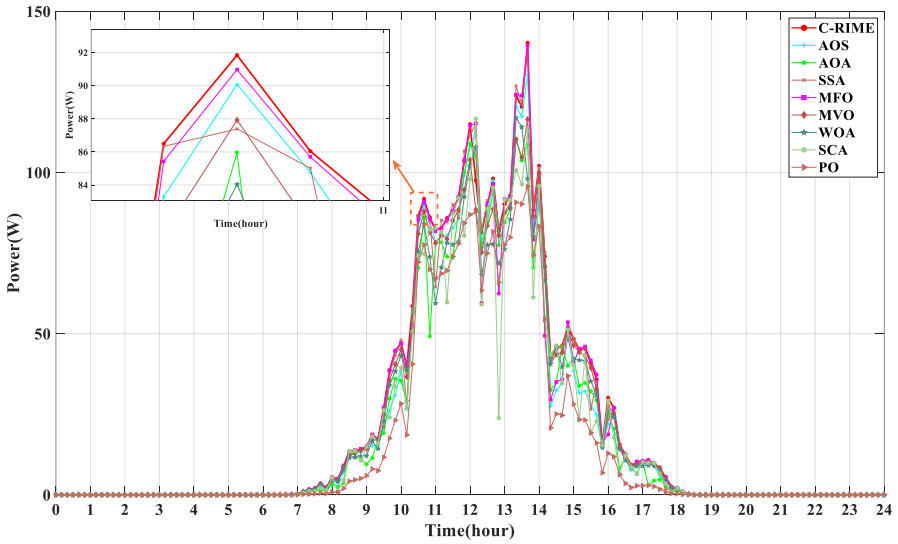
C-RIME
AOS
AOA
SSA
MFO
MVO
WOA
SCA
PO
Power(W)
Time(hour)

(a)

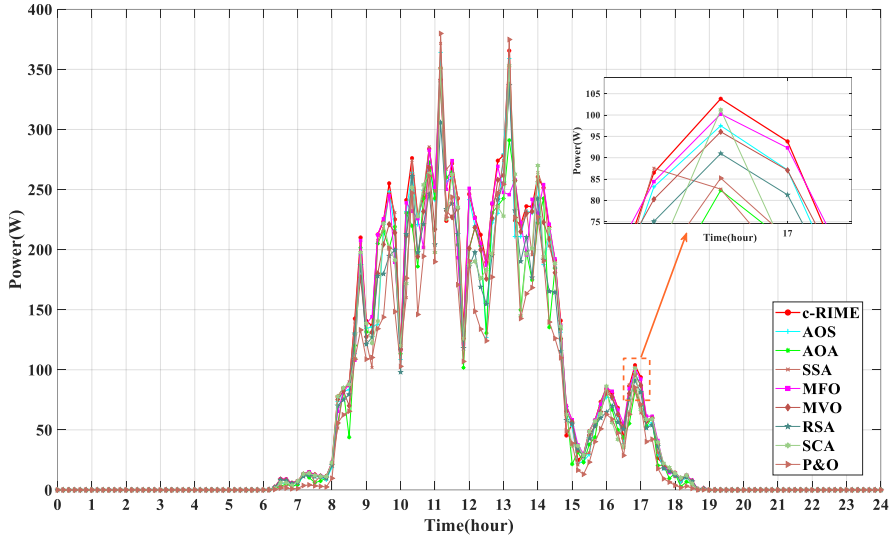
c-RIME
AOS
AOA
SSA
MFO
MVO
RSA
SCA
P&O
Power(W)
Time(hour)

(b)

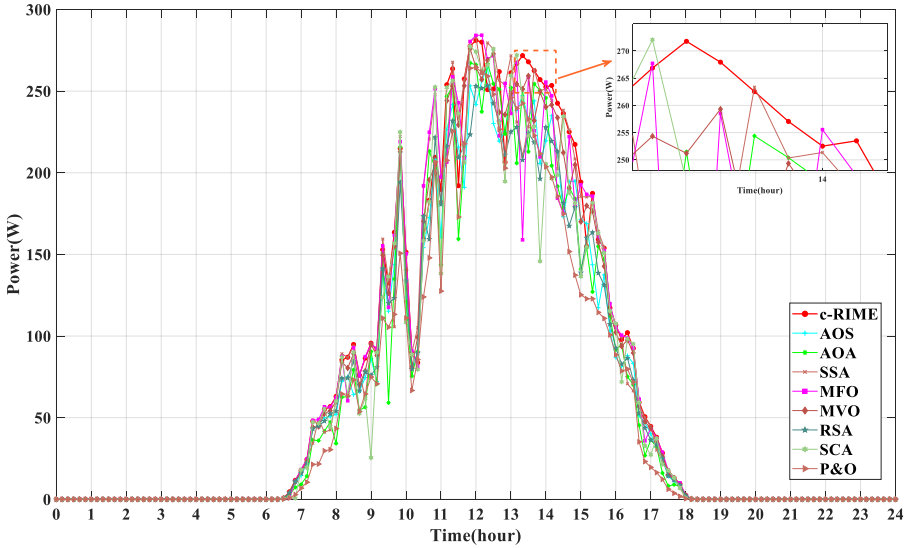
c-RIME
AOS
AOA
SSA
MFO
MVO
RSA
SCA
P&O
Power(W)
Time(hour)

(c)

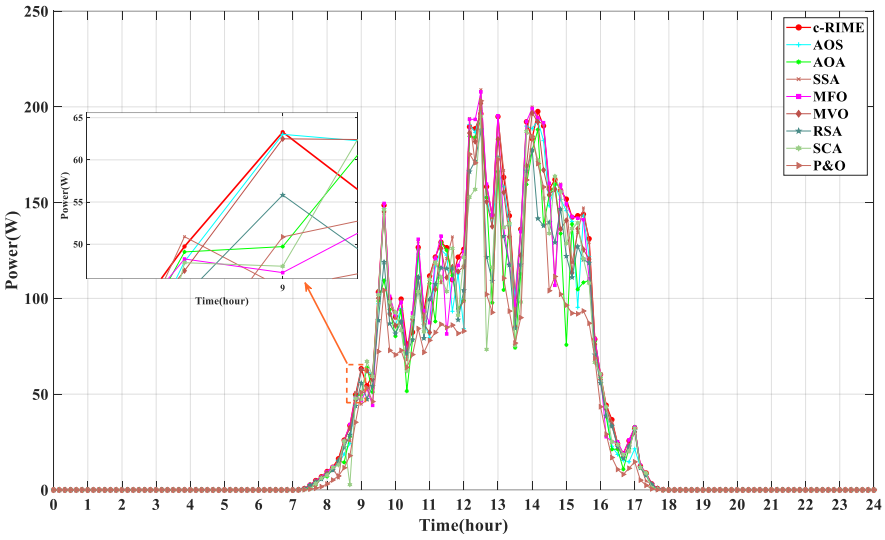

(d)

Fig. 17. Power obtained under four different typical days in Hong Kong. (a) Spring, (b) Summer, (c) Autumn, and (d) Winter.

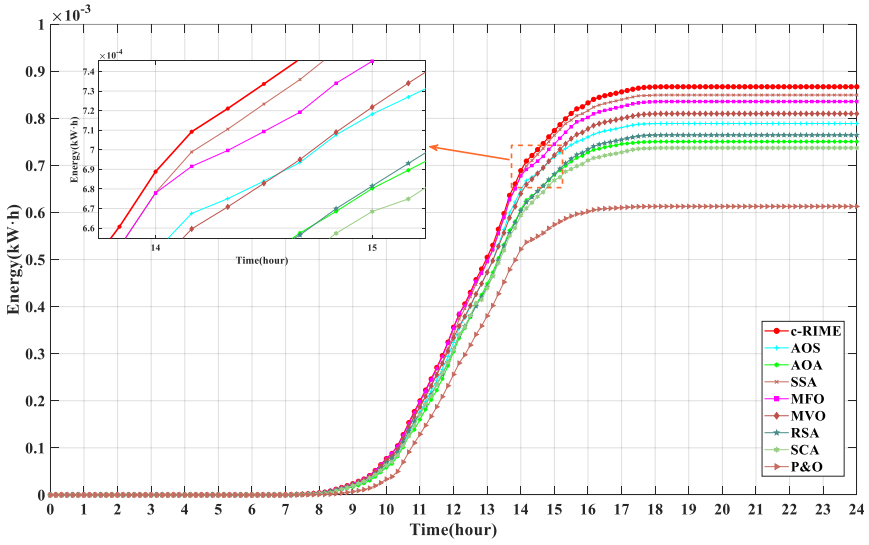

(a)

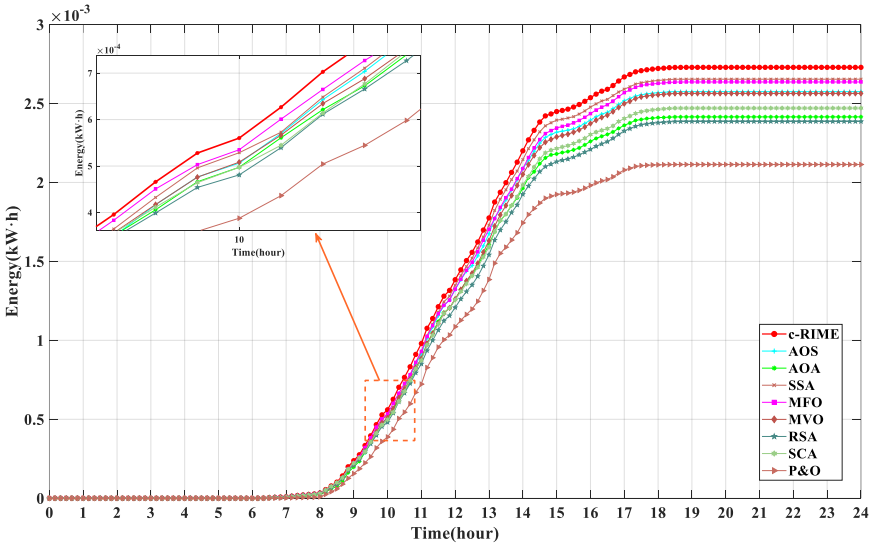

(b)

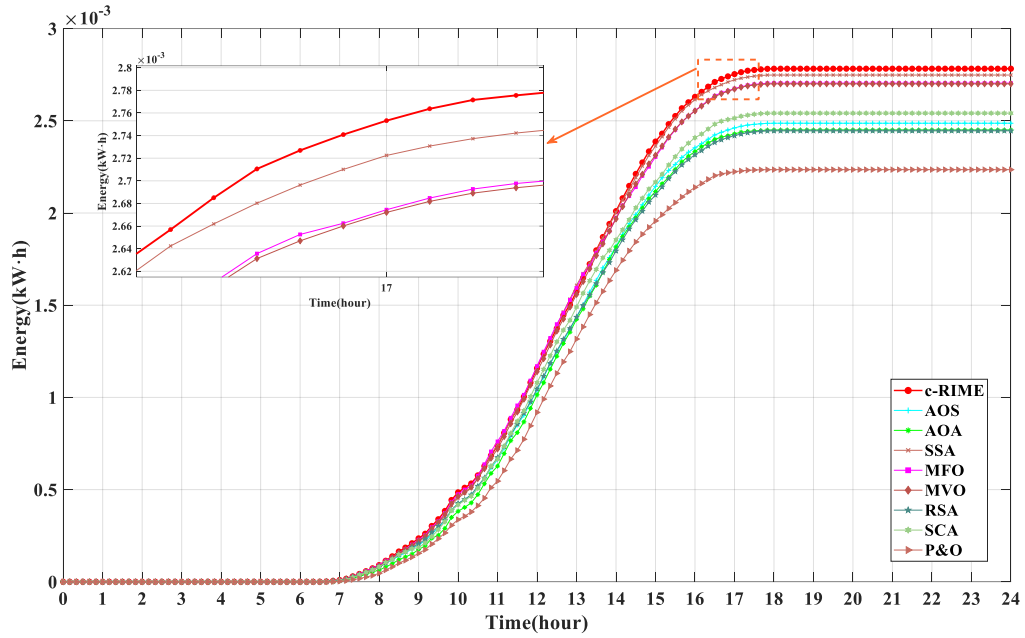

(c)

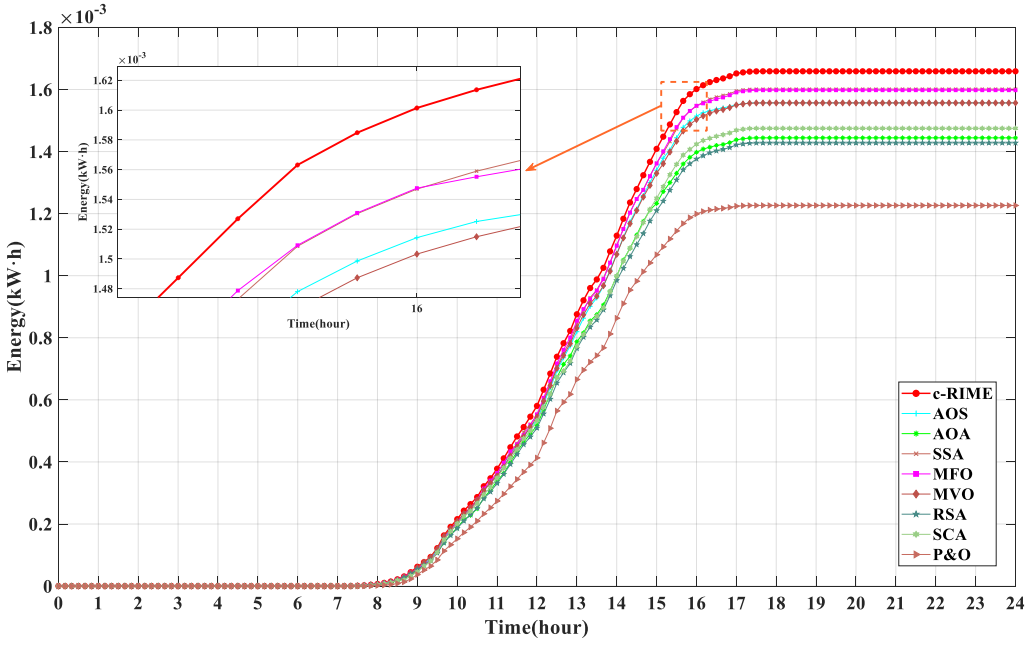

(d)

Fig. 18. Energy obtained by ten MPPT techniques under four different typical days in Hong Kong. (a) Spring, (b) Summer, (c) Autumn, and (d) Winter.

5. Techno-environmental assessment

This section presents a systematic techno-environmental analysis, aiming to not only evaluate the energy enhancement performance of the PV-TEG system after MPPT, but also discuss its environmental benefits, emphasizing the importance of incorporating carbon emission analysis into the research and assessment of renewable energy technologies.

5.1 Technical assessment

In this section, the performance analysis tends to focus on the technical aspects of the simulation results, which are crucial to understanding the performance dynamics of various MPPT strategies under various operating conditions and thus gaining insights into their efficiency and stability. The focus of this analysis is the energy output under different operating scenarios, which is the most critical indicator to measure the MPPT scheme's ability to improve energy conversion under adverse operating conditions. In addition, the maximum and average fluctuations of power output, represented by $\Delta v^{\max}$ and Δv^{avg}, are employed as evaluation indicators representing the system's operational stability, defined by

$$\Delta v^{\text{avg}} = \frac{1}{T-1}\sum_{t=2}^{T} \frac{|P_{\text{out}}(t)-P_{\text{out}}(t-1)|}{P_{\text{out}}^{\text{avg}}} \tag{30}$$

$$\Delta v^{\max} = \max_{t=2,3,\cdots,T} \frac{|P_{\text{out}}(t)-P_{\text{out}}(t-1)|}{P_{\text{out}}^{\text{avg}}} \tag{31}$$

where T and t respectively indicate the total and current operation time and $P_{\text{out}}^{\text{avg}}$ represents the average power output of the PV-TEG system throughout the entire operational period.

Table 4 shows the statistical outcomes derived from the application of various MPPT strategies on PV-TEG hybrid systems, covering nine distinctive approaches within four afore-discussed testing environments. It is noteworthy that P&O is excluded from this comparison, which is due to the methods' tendency to quickly fall into local optimum during the initial phase of seeking the maximum power point. As a result, it exhibits minimal fluctuations, but this is attributed to its premature convergence, which is evident from Figs. 10, 12, 14, 17, and 18, where the energy extracted by P&O is among the lowest under various testing conditions. Consequently, the power fluctuation metrics for P&O do not provide meaningful reference value and are therefore excluded from the comparison to avoid misleading readers. Here, the output energy output of P&O under various scenarios is listed separately: 149.99 and 786.09 W·s for startup test and stepwise variations in irradiation, respectively; 2.0679, 0.6128, 2.1135, 2.2351, 1.2263 10^{-3}kW·h for stochastic change in irradiation, spring, summer, autumn, and winter day in Hong Kong, respectively. From Table 4, it can be seen that across all testing scenarios, c-RIME consistently shows the highest energy output, indicating its superior ability to optimize energy conversion under varying operational conditions. For instance, in the startup test, the output energy of c-RIME is 146.49%, 119.58%, 106.90%, 104.12%, 102.76%, 101.99%, 126.67%, and 103.16% to that of P&O, SCA, RSA, MVO, MFO, SSA, AOA, and AOS, respectively. In particular, this trend is consistent across the seasonal data collected in Hong Kong, verifying its effectiveness in real-world environmental conditions. For instance, the output energy obtained by c-RIME under the winter day is 135.25%, 112.46%, 116.16%, 106.54%, 103.81%, 103.59%, 114.85%, and 106.53% to that of P&O, SCA, RSA, MVO, MFO, SSA, AOA, and AOS, respectively. Meanwhile, c-RIME generally exhibits lower fluctuation metrics compared to other methods, signifying better operational stability. For example, during the start-up test, c-RIME's $\Delta v^{\max}$ is 12.99% while Δv^{avg} following a similar pattern, which is significantly lower than other methods, reflecting its capacity to maintain stable operation under uneven distribution in solar irradiation conditions. While c-RIME consistently delivers the highest energy output, its fluctuation indicators are not always the lowest since c-RIME prioritizes energy capture over absolute stability. However, its fluctuations remain within a reasonable range, suggesting a balanced approach to maximizing energy yield while maintaining system stability.

Table 4. Statistical results of various methods under four case studies

Testing scenarios		Indicators	SCA	RSA	MVO	MFO	SSA	AOA	AOS	c-RIME
Start-up test		Energy(W·s)	183.74	205.54	211.03	213.82	215.44	173.47	212.99	219.72
		$\Delta v^{\max}$(%)	30.0100	34.6369	35.1643	21.1106	32.3056	39.4998	26.7512	12.9878
		Δv^{avg}(%)	0.2310	0.4550	0.4580	0.3053	0.1757	0.2004	0.3527	0.1513
Stepwise variations in solar irradiation		Energy(W·s)	830.83	906.44	928.42	900.4781	943.98	918.03	939.64	957.72
		$\Delta v^{\max}$(%)	34.6273	34.4243	23.4959	26.7158	26.3940	33.0741	28.9016	20.2471
		Δv^{avg}(%)	0.5496	0.5682	0.3419	0.4774	0.4927	0.7601	0.5893	0.3203
Stochastic change in solar irradiation		Energy(10^{-3}kW·h)	2.2945	2.2459	2.3969	2.4881	2.5257	2.1886	2.4194	2.5834
		$\Delta v^{\max}$(%)	35.5567	37.4670	30.1188	26.8605	24.9954	31.0313	29.6441	22.5967
		Δv^{avg}(%)	1.4053	1.4129	0.9026	0.4280	0.3557	0.3973	0.6630	0.3383
Field measured temperature and solar		Energy(10^{-3}kW·h)	0.7373	0.7646	0.8099	0.8357	0.8476	0.7506	0.7891	0.8672
irradiation data in Hong Kong	**Spring**	$\Delta v^{\max}$	7.9207	6.2128	6.9227	10.9795	8.3556	5.3814	11.5727	9.7217
		Δv^{avg}	0.0480	0.0776	0.0431	0.0548	0.0397	0.0214	0.0735	0.0382
		Energy(10^{-3}kW·h)	2.4708	2.3860	2.5637	2.6361	2.6537	2.4150	2.5750	2.7287
	Summer	$\Delta v^{\max}$	7.1022	4.9077	5.5565	6.8977	6.5836	4.8425	9.5050	9.2736
		Δv^{avg}	0.0459	0.0699	0.0324	0.0354	0.0421	0.0285	0.0618	0.0485
		Energy(10^{-3}kW·h)	2.5415	2.4456	2.7005	2.7045	2.7481	2.4499	2.4869	2.7826
	Autumn	$\Delta v^{\max}$	9.7391	6.7597	7.4047	9.1448	9.0798	5.8054	6.9300	8.9688
		Δv^{avg}	0.0571	0.0917	0.0492	0.0435	0.0404	0.0440	0.0888	0.0397
		Energy(10^{-3}kW·h)	1.4748	1.4279	1.5568	1.5977	1.6011	1.4441	1.5569	1.6586
	Winter	$\Delta v^{\max}$	10.5568	7.3548	8.1969	11.3000	8.1821	6.8893	13.5449	9.1496
		Δv^{avg}	0.0628	0.0949	0.0524	0.0499	0.0397	0.0369	0.0872	0.0340

5.2 Environmental assessment

The essence and motivation behind developing various renewable energy technologies lie in transitioning from traditional energy structures to reduce environmental impact, foster sustainable development, and accelerate progress towards Net Zero goals. However, a substantial gap exists in previous research regarding comprehensive environmental analysis of these systems. The energy sector stands as the world's largest carbon emitter, with traditional power plants, predominantly coal-fired and gas-fired units, significantly contributing to atmospheric pollution and extensive emissions of greenhouse gases. While the carbon capture, utilization, and storage (CCUS) technique has been implemented in coal-fired and gas-fired units to reduce CO_2 emissions, their carbon footprint remains significantly larger compared to purely renewable energy systems.

Meanwhile, the application for PV-TEG hybrid systems is still under the research and development stage without large-scale commercial application, thus specific data on their combined carbon emissions are still blank. In this context, this research chooses to base its environmental analysis on the available data from standalone PV systems. Additionally, given that the contribution of the TEG part to the whole system's power production is relatively minor (e.g., only one-thirtieth of the PV system's power generation capacity), the inclusion of TEG, while it does impact the system's overall energy efficiency and carbon emissions, is anticipated to have a marginal effect when considering the scale of its contribution. Thus, given the constraints of current data and research, utilizing data from standalone PV systems for environmental analysis is a reasonable and practical approach. This method can provide valuable insights into the potential contributions of the PV component of the hybrid system toward reducing carbon emissions. To this end, a comprehensive comparative assessment framework is designed incorporating the carbon emission factors of different fuel types for electricity generation, which include PV power generation, coal-fired, coal-fired with CCUS, gas-fired with CCUS, and general power grid emission factors. The method for calculating carbon reduction benefits is detailed as: Based on the optimized PV energy output, the carbon reduction benefits are derived by comparing the carbon emission factors of various types of electricity generation with the carbon emission factor of PV power generation [49], as follows:

$$RCE = E_{\text{gen}} \times EF_{\text{pv}} - E_{\text{gen}} \times EF_{\text{other}} \tag{32}$$

where RCE denotes the reduced carbon emissions, E_{gen} denotes the energy output, EF_{pv} signifies the PV system's carbon emission factor, and EF_{other} denotes the carbon emission factor of other fuel types for electricity generation.

This work employs the real yearly output power data from a PV station located in Ningxia Hui Autonomous Region in China for calculation, whose installation capacity is 130 kW. The PV power generation curve of this PV station throughout the whole year of 2022 is demonstrated in Fig. 19, with a data sampling interval of 15 minutes. Besides, according to the technical results, the proposed c-RIME can considerably improve the output energy compared with the traditional P&O method which serves as the most commonly used MPPT strategy in China's real-life PV stations across different regions and system scales. Considering the differences in location and the corresponding atmospheric conditions, this section employs the average energy enhancement ratio of c-RIME to P&O. According to the PV output data, the total output energy of this PV station can be further calculated, with the result of 210336.30 and 277818.36 kWh using P&O and c-RIME MPPT strategy, respectively. Additionally, it should be noted

that since the MPPT algorithm proposed is suitable for black-box scenarios, it can be generalized as a universal MPPT strategy for the system studied.

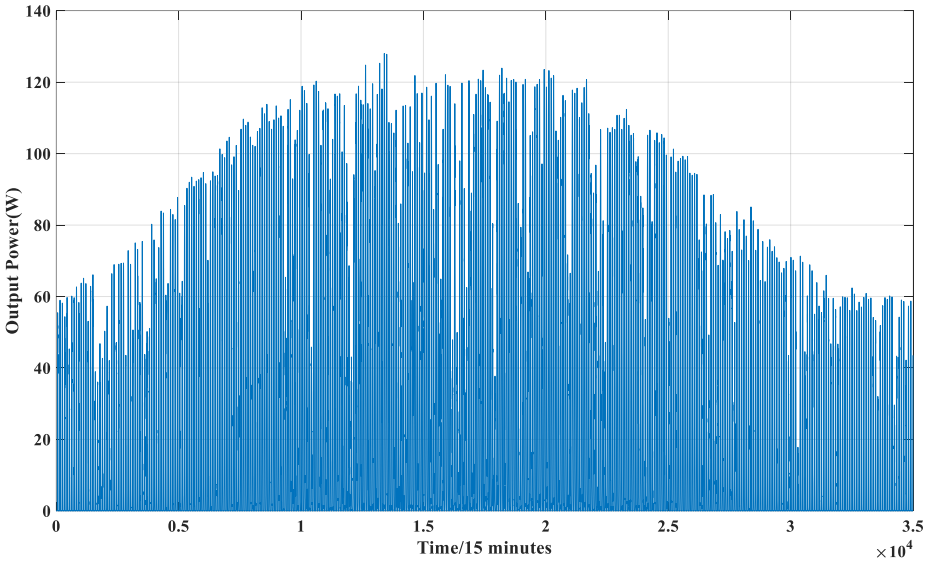

Fig. 19. Power output of a PV station in China with a capacity of 130 kW in 2022.

Based on the reported carbon emission data in literature [50-53], Table 5 presents a detailed analysis of carbon emissions based on various benchmark categories for electricity generation in China, all compared under the same condition of generating 277818.36 kWh of electricity. Table 5 clearly illustrates that compared to traditional and even some modernized fossil fuel-based technologies, optimized PV technology can significantly reduce carbon emissions. In detail, compared with coal-fired, coal-fired with CCUS, gas-fired with CCUS, and China national grid's average emission factors, PV power generation equipped with efficient MPPT technique can achieve a significant RCE of 278373.998 kg, 243646.702 kg, 108904.797 kg, and 158356.465 kg. This emphasizes the environmental benefits of developing and implementing PV technologies, which are crucial for promoting net-zero initiatives and mitigating climate change impacts.

Table 5. Carbon emission evaluation results

Benchmark category	**Technology type**	**CO_2 emission factor for electricity generation (kg CO_2/kWh)**	**Total CO_2 emission (kg)**
Coal-fired	Conventional high-pressure coal-fired units	1.063	295320.917
units	Coal with CCUS	0.877	243646.702
Gas-fired units	Gas with CCUS	0.392	108904.797
Power grid	Average emissions of China's national power grid	0.570	158356.465
PV system	PV system with c-RIME MPPT	0.061	16946.919

To summarize, considering both technical and environmental results, it can be concluded that the developed MPPT technology continuously maintains the system's operation at its optimal power point, regardless of changing environmental circumstances. This means that more electricity can be generated from the same area of PV panels compared to systems without MPPT technology or less effective MPPT technologies, lowering the carbon intensity of electricity production. Meanwhile, the environmental benefits of PV power generation have been evidenced in Table 5. In general, proper MPPT technology

can further enhance the performance and reliability of PV systems, facilitating the incorporation of a larger share of renewable energy sources into the power grid to replace traditional fossil fuel generation. The reduction in fossil fuel use and associated carbon emissions, coupled with an increase in green energy's share, promotes the energy structure's optimization and transition towards lower carbon footprints.

6. Conclusions

This work designs a hybrid PV-TEG system as a viable approach for improving the energy conversion efficiency and operational reliability of standalone PV systems. To address the operational challenges posed by PSCs and NTD, a c-RIME based MPPT technique is developed specifically for the hybrid system, aiming at dynamically extracting the optimal output energy while reducing system carbon emissions under diverse operation scenarios. The core contributions and novelties of this work are summarized below:

(1) To more efficiently utilize captured solar energy and realize waste heat cyclic utilization, this work combines individual PV and TEG systems for a mutually beneficial power generation configuration. The waste heat produced during PV power generation can be transferred to TEG modules for its electricity generation, meanwhile, this heat dissipation process supported by the passive cooling from TEG modules can in turn lower the operating temperature of PV systems, thus improving energy conversion efficiency and slow down its degradation;

(2) A powerful MPPT control scheme is developed based on c-RIME to mitigate the unfavorable effects of PSCs, ensuring that the system can always generate maximum power under various adverse operating conditions, enhancing operational reliability and economic efficiency;

(3) To comprehensively verify the performance of the proposed MPPT strategy, four different case studies are designed involving various irradiance and temperature variation patterns. In particular, tests using real-world atmospheric data collected from Hong Kong validate the robustness and applicability of the devised MPPT strategy under real-life environmental conditions;

(4) To fill up the gap, this work not only focuses on the technical performance of the MPPT implementation but also carries out a critical environmental benefits analysis by employing the LCA and real-world carbon emission factors across various benchmarks for electricity production. Based on this, the carbon reduction performance can be comprehensively and qualitatively evaluated, which is crucial for understanding and minimizing the carbon footprint of these renewable energy technologies. In general, simulation results indicate that from the technical perspective, the proposed c-RIME based MPPT technique allows for the highest energy yield among tested MPPT strategies under all testing scenarios. For instance, the output energy of c-RIME is 124.93%, 112.59%, 115.03%, 107.78%, 103.83%, 102.28%, 118.04%, and 106.78% to that of P&O, SCA, RSA, MVO, MFO, SSA, AOA, and AOS, respectively. Further, the environmental assessment reveals that c-RIME not only leads to an increase in energy efficiency but also plays a crucial role in reducing the carbon emissions caused by electricity generation, contributing to broader goals of mitigating climate change and promoting environmental sustainability.

Considering the current deficiencies in this work, future study tends to move toward the following two aspects:

(a) Refined system configuration and reduced control complexity: At the current stage, this work

still needs to employ two DC-DC converters with two separate controllers to realize control purposes and boost harvested output power, which can ensure high control reliability but also increase the cost and complexity. To improve this, future work will further investigate how to more efficiently and cost-effectively realize hybrid PV-TEG coupling configuration, thus reducing the costs and complexity of the control part;

(b) When calculating carbon reduction benefits, a simplified analysis approach is employed. Although this approach is sufficient to support and reflect the real characteristics and trends of results, future research will keep focusing on collecting and analyzing actual operational data from PV-TEG hybrid systems by integrating real-world hardware platforms or even operational pilots, thus offering a more authentic reflection of carbon footprints. This would enable a more precise evaluation of the environmental performance of this emerging technology and further explore its potential applications in the sustainable energy field.

Acknowledgments

This work is supported by the National Natural Science Foundation of China (62263014), Yunnan Provincial Basic Research Project (202401AT070344, 202301AT070443).

References

[1] Jin, C., Lv, Z., Li, Z., & Sun, K. (2023). Green finance, renewable energy and carbon neutrality in OECD countries. *Renewable Energy*, *211*, 279-284.

[2] Liu, J., Zhao, H., Wang, S., Liu, G., Zhao, J., & Dong, Z. Y. (2023). Real-time emission and cost estimation based on unit-level dynamic carbon emission factor. *Energy Conversion and Economics*, *4*(1), 47-60.

[3] Dong, F., Li, Y., Gao, Y., Zhu, J., Qin, C., & Zhang, X. (2022). Energy transition and carbon neutrality: Exploring the non-linear impact of renewable energy development on carbon emission efficiency in developed countries. *Resources, Conservation and Recycling*, *177*, 106002.

[4] Grover, H., Verma, A., & Bhatti, T. S. (2023). A fast and robust DOBC based frequency and voltage regulation scheme for future power systems with high renewable penetration. *Energy Conversion and Economics*, *4*(4), 287-302.

[5] Yang, B., Wang, J., Zhang, X., Yu, T., Yao, W., Shu, H., Zeng, F., Sun, L. (2020). Comprehensive overview of meta-heuristic algorithm applications on PV cell parameter identification. *Energy Conversion and Management*, *208*, 112595.

[6] Fan, S., Wang, Y., Cao, S., Sun, T., & Liu, P. (2021). A novel method for analyzing the effect of dust accumulation on energy efficiency loss in photovoltaic (PV) system. *Energy*, *234*, 121112.

[7] Amalu, E. H., & Fabunmi, O. A. (2022). Thermal control of crystalline silicon photovoltaic (c-Si PV) module using Docosane phase change material (PCM) for improved performance. *Solar Energy*, *234*, 203-221.

[8] Yin, Z., Zhang, T., Cai, J., Fan, Y., & Shi, Z. (2023). Investigation on the operating characteristics of a directly-attached light crystalline silicon PV roof. *Solar Energy*, *262*, 111849.

[9] Jamali, E., Nobakhti, M. H., Ziapour, B. M., & Khayat, M. (2023). Performance analysis of a novel model of photovoltaic PV-TEGs system enhanced with flat plate mirror reflectors. *Energy Conversion and Management*, *279*, 116766.

[10] Babu, C., & Ponnambalam, P. (2018). The theoretical performance evaluation of hybrid PV-TEG system. *Energy conversion and management*, *173*, 450-460.

[11] Fini, M. A., Gharapetian, D., & Asgari, M. (2022). Efficiency improvement of hybrid PV-TEG system based on an energy, exergy, energy-economic and environmental analysis; experimental, mathematical and numerical approaches. *Energy Conversion and Management*, *265*, 115767.

[12] De Luca, D., Strazzullo, P., Di Gennaro, E., Caldarelli, A., Gaudino, E., Musto, M., & Russo, R. (2023). High vacuum flat

plate photovoltaic-thermal (HV PV-T) collectors: Efficiency analysis. *Applied Energy*, *352*, 121895.

[13] Yang, B., Zhang, M., Zhang, X., Wang, J., Shu, H., Li, S., He, T., Yang, L., & Yu, T. (2020). Fast atom search optimization based MPPT design of centralized thermoelectric generation system under heterogeneous temperature difference. *Journal of Cleaner Production*, *248*, 119301.

[14] Tyagi, K., Gahtori, B., Kumar, S., & Dhakate, S. R. (2023). Advances in solar thermoelectric and photovoltaic-thermoelectric hybrid systems for power generation. *Solar Energy*, *254*, 195-212.

[15] Qasim, M. A., Velkin, V. I., & Shcheklein, S. E. (2023). Experimental study on hybridization of a PV–TEG system for electrical performance enhancement using heat exchangers, energy, exergy and economic levelized cost of energy (LCOE) analysis. *Clean Energy*, *7*(4), 808-823.

[16] Babu, C., & Ponnambalam, P. (2017). The role of thermoelectric generators in the hybrid PV/T systems: A review. *Energy conversion and management*, *151*, 368-385.

[17] Skoplaki, E. P. J. A., & Palyvos, J. A. (2009). Operating temperature of photovoltaic modules: A survey of pertinent correlations. *Renewable energy*, *34*(1), 23-29.

[18] Yang, B., Wu, S., Li, Q., Yan, Y., Li, D., Luo, E., Zeng, C., Chen, Y., Guo, Z., Shu, H., Li, Z., & Wang, J. (2023). Jellyfish search algorithm based optimal thermoelectric generation array reconfiguration under non-uniform temperature distribution condition. *Renewable Energy*, *204*, 197-217.

[19] Bollipo, R. B., Mikkili, S., & Bonthagorla, P. K. (2020). Critical review on PV MPPT techniques: classical, intelligent and optimisation. *IET Renewable Power Generation*, *14*(9), 1433-1452.

[20] Yang, B., Zhu, T., Wang, J., Shu, H., Yu, T., Zhang, X., ... & Sun, L. (2020). Comprehensive overview of maximum power point tracking algorithms of PV systems under partial shading condition. *Journal of Cleaner Production*, *268*, 121983.

[21] Yang, B., Yu, T., Zhang, X., Li, H., Shu, H., Sang, Y., & Jiang, L. (2019). Dynamic leader based collective intelligence for maximum power point tracking of PV systems affected by partial shading condition. *Energy Conversion and Management*, *179*, 286-303.

[22] Eltamaly, A. M. (2021). A novel musical chairs algorithm applied for MPPT of PV systems. *Renewable and Sustainable Energy Reviews*, *146*, 111135.

[23] Yang, B., Xie, R., Duan, J., & Wang, J. (2023). State-of-the-art review of MPPT techniques for hybrid PV-TEG systems: Modeling, methodologies, and perspectives. *Global Energy Interconnection*, *6*(5), 567-591.

[24] Mohanty, S., Subudhi, B., & Ray, P. K. (2016). A grey wolf-assisted perturb & observe MPPT algorithm for a PV system. *IEEE Transactions on Energy Conversion*, *32*(1), 340-347.

[25] Motahhir, S., Chalh, A., El Ghzizal, A., & Derouich, A. (2018). Development of a low-cost PV system using an improved INC algorithm and a PV panel Proteus model. *Journal of Cleaner production*, *204*, 355-365.

[26] Refaat, A., Ali, Q. A., Elsakka, M. M., Elhenawy, Y., Majozi, T., Korovkin, N. V., & Elfar, M. H. (2024). Extraction of maximum power from PV system based on horse herd optimization MPPT technique under various weather conditions. *Renewable Energy*, *220*, 119718.

[27] Zhang, X., Yang, B., Yu, T., & Jiang, L. (2020). Dynamic Surrogate Model based optimization for MPPT of centralized thermoelectric generation systems under heterogeneous temperature difference. *IEEE Transactions on Energy Conversion*, *35*(2), 966-976.

[28] Salim, J. A., Albaker, B. M., Alwan, M. S., & Hasanuzzaman, M. (2022). Hybrid MPPT approach using Cuckoo Search and Grey Wolf Optimizer for PV systems under variant operating conditions. *Global Energy Interconnection*, *5*(6), 627-644.

[29] Sarvi, M., & Azadian, A. (2022). A comprehensive review and classified comparison of MPPT algorithms in PV systems. *Energy Systems*, *13*(2), 281-320.

[30] Khan, N. M., Mansoor, M., Mirza, A. F., Moosavi, S. K. R., Qadir, Z., & Zafar, M. H. (2022). Energy harvesting and stability analysis of centralized TEG system under non-uniform temperature distribution. *Sustainable Energy Technologies and*

Assessments, *52*, 102028.

[31] Khan, M. K., Zafar, M. H., Mansoor, M., Mirza, A. F., Khan, U. A., & Khan, N. M. (2022). Green energy extraction for sustainable development: A novel MPPT technique for hybrid PV-TEG system. *Sustainable Energy Technologies and Assessments*, *53*, 102388.

[32] Mirza, A. F. , Mansoor, M., Zerbakht, K., Javed, M. Y., Zafar, M. H., & Khan, N. M. (2021). High-efficiency hybrid PV-TEG system with intelligent control to harvest maximum energy under various non-static operating conditions. *Journal of Cleaner Production*, *320*, 128643.

[33] Yang, B., Wu, S., Huang, J., Guo, Z., Wang, J., Zhang, Z., ... & Jiang, L. (2023). Salp swarm optimization algorithm based MPPT design for PV-TEG hybrid system under partial shading conditions. *Energy Conversion and Management*, *292*, 117410.

[34] Verma, V., Kane, A., & Singh, B. (2016). Complementary performance enhancement of PV energy system through thermoelectric generation. *Renewable and Sustainable Energy Reviews*, *58*, 1017-1026.

[35] Saleh, U. A., Johar, M. A., Jumaat, S. A. B., Rejab, M. N., & Jamaludin, W. A. W. (2021). Evaluation of a PV-TEG hybrid system configuration for an improved energy output: a review. *International Journal of Renewable Energy Development*, *10*(2), 385.

[36] El-Dabah, M. A., El-Sehiemy, R. A., Hasanien, H. M., & Saad, B. (2023). Photovoltaic model parameters identification using Northern Goshawk Optimization algorithm. *Energy*, *262*, 125522..

[37] Muzathik, A. M. (2014). Photovoltaic modules operating temperature estimation using a simple correlation. *International Journal of Energy Engineering*, *4*(4), 151.

[38] Bingöl, O., & Özkaya, B. (2018). Analysis and comparison of different PV array configurations under partial shading conditions. *Solar Energy*, *160*, 336-343.

[39] Wang, J., Yang, B., Li, D., Zeng, C., Chen, Y., Guo, Z., ... & Yu, T. (2021). Photovoltaic cell parameter estimation based on improved equilibrium optimizer algorithm. *Energy Conversion and Management*, *236*, 114051.

[40] Liu, Y. H., Chiu, Y. H., Huang, J. W., & Wang, S. C. (2016). A novel maximum power point tracker for thermoelectric generation system. *Renewable Energy*, *97*, 306-318.

[41] Su, H., Zhao, D., Heidari, A. A., Liu, L., Zhang, X., Mafarja, M., & Chen, H. (2023). RIME: A physics-based optimization. *Neurocomputing*, *532*, 183-214.

[42] Vieira, R. S., & Mosna, R. A. (2022). Homoclinic chaos in the Hamiltonian dynamics of extended test bodies. *Chaos, Solitons & Fractals*, *163*, 112541.

[43] Varol Altay, E., & Alatas, B. (2020). Bird swarm algorithms with chaotic mapping. *Artificial Intelligence Review*, *53*(2), 1373-1414.

[44] Raiker, G. A., & Loganathan, U. (2021). Current control of boost converter for PV interface with momentum-based perturb and observe MPPT. *IEEE Transactions on Industry Applications*, *57*(4), 4071-4079.

[45] Abualigah, L., Abd Elaziz, M., Sumari, P., Geem, Z. W., & Gandomi, A. H. (2022). Reptile Search Algorithm (RSA): A nature-inspired meta-heuristic optimizer. *Expert Systems with Applications*, *191*, 116158.

[46] Mirjalili, S., Mirjalili, S. M., & Hatamlou, A. (2016). Multi-verse optimizer: a nature-inspired algorithm for global optimization. *Neural Computing and Applications*, *27*, 495-513.

[47] Mirjalili, S. (2015). Moth-flame optimization algorithm: A novel nature-inspired heuristic paradigm. *Knowledge-based systems*, *89*, 228-249.

[48] Mirjalili, S. (2016). SCA: a sine cosine algorithm for solving optimization problems. *Knowledge-based systems*, *96*, 120-133.

[49] Singh, N. K., Goswami, A., & Sadhu, P. K. (2023). Energy economics and environmental assessment of hybrid hydel-floating solar photovoltaic systems for cost-effective low-carbon clean energy generation. *Clean Technologies and Environmental*

Policy, *25*(4), 1339-1360.

[50] An, M., & Sun, X. (2024). Carbon footprints of solar panels in China provinces based on different production and waste treatment scenarios. *Journal of Cleaner Production*, *435*, 140453.

[51] Guo, X., Dong, Y., & Ren, D. (2023). CO2 emission reduction effect of photovoltaic industry through 2060 in China. *Energy*, *269*, 126692.

[52] International Energy Agency (IEA). (2022). Enhancing China's ETS for Carbon Neutrality: Focus on Power Sector.

[53] Zhang, S., Zhang, J., Bu, F., Cheng, L., Wang, Z., & Gao, Z. (2023). A Practical Method for Calculating Indirect Carbon Emissions of Electricity Users in Large Power Grid. In *International Conference on Wireless Power Transfer* (pp. 45-55). Singapore: Springer Nature Singapore.